Optimized interatomic potential for silicon and its application to thermal stability of silicene

G. P. Purja Pun and Y. Mishin
Department of Physics and Astronomy, MSN 3F3, George Mason University, Fairfax, Virginia 22030, USA
(Received 26 March 2017; published 12 June 2017)

An optimized interatomic potential has been constructed for silicon using a modified Tersoff model. The potential reproduces a wide range of properties of Si and improves over existing potentials with respect to point defect structures and energies, surface energies and reconstructions, thermal expansion, melting temperature, and other properties. The proposed potential is compared with three other potentials from the literature. The potentials demonstrate reasonable agreement with first-principles binding energies of small Si clusters as well as single-layer and bilayer silicenes. The four potentials are used to evaluate the thermal stability of free-standing silicenes in the form of nanoribbons, nanoflakes, and nanotubes. While single-layer silicene is found to be mechanically stable at zero Kelvin, it is predicted to become unstable and collapse at room temperature. By contrast, the bilayer silicene demonstrates a larger bending rigidity and remains stable at and even above room temperature. The results suggest that bilayer silicene might exist in a free-standing form at ambient conditions.

DOI: 10.1103/PhysRevB.95.224103

I. INTRODUCTION

Silicon is one of the most important functional materials widely used in electronic, optical, energy conversion, and many other applications. Not surprisingly, Si has been the subject of many classical molecular dynamics (MD) and other large-scale atomistic computer studies for almost three decades. Although classical atomistic simulations cannot access electronic or magnetic properties, they are indispensable for gaining a better understanding of the atomic structures, thermal and mechanical properties of the crystalline, liquid, and amorphous Si and various nanoscale objects such as nanowires and nanodots. Atomistic simulations rely on semiempirical interatomic potentials. The accuracy of the results delivered by atomistic simulations depends critically on the reliability of interatomic potentials.

Several dozen semiempirical potentials have been developed for Si. Although none of them reproduces all properties accurately, there is a trend towards a gradual improvement in their reliability as more sophisticated potential generation methods are developed and larger experimental and first-principles datasets become available for the optimization and testing. The most popular Si potentials were proposed by Stillinger and Weber (SW) [1] and Tersoff [2–4]. The original Tersoff potentials were modified by several authors by slightly changing the analytical functions and improving the optimization [5–10]. Other Si potential formats include the environment-dependent interatomic potential [11], the modified embedded atom method (MEAM) potentials [12–18], and bond-order potentials [19,20].

One of the most significant drawbacks of the existing Si potentials is the overestimation of the melting temperature T_m, in many cases by hundreds of degrees. Other typical problems include underestimated vacancy and surface energies and positive Cauchy pressure ($c_{12} - c_{44}$), which in reality is negative (c_{ij} being elastic constants). Kumagai *et al.* [7] constructed a significantly improved Tersoff potential that predicts $T_m = 1681$ K in close agreement with the experimental value of 1687 K, gives the correct Cauchy pressure, and is accurate with respect to many other properties. This potential, usually referred to as MOD [7], is probably the most advanced Tersoff-type potential for Si available today. However, it still suffers from a low vacancy formation energy, low surface energies, and overestimated thermal expansion at high temperatures and the volume effect of melting.

The goal of this work was twofold. The first goal was to further improve on the MOD potential [7] by addressing its shortcomings with a minimal impact on other properties. This was achieved by slightly modifying the potential format and performing a deeper optimization. When testing the new potential, we compare it not only with MOD but also with the popular SW potential [1]. We further include the MEAM potential developed by Ryu *et al.* [14] to represent a different potential format. To our knowledge, this is the only MEAM potential whose melting point is close to experimental.

The second goal was to test the four potentials for their ability to predict the energies of low-dimensional structures, such as small Si clusters and single- and double-layer forms of silicene (2D allotrope of Si). Si potentials are traditionally considered to be incapable of reproducing low-dimensional structures. This view is largely based on testing the SW potential. The MOD and MEAM potentials have not been tested for the properties of clusters or silicenes in any systematic manner. Such tests were conducted in this work using all four potentials. The results suggest that the present potential, MOD, and MEAM do capture the main trends and in many cases agree with first-principles density functional theory (DFT) calculations. As such, they can be suitable for exploratory studies of thermal and mechanical stability of Si clusters and 2D structural forms of Si. In this work, we apply them to evaluate the stability of free-standing single-layer and bilayer silicenes at room temperature.

II. POTENTIAL GENERATION PROCEDURES

The total energy of a collection of atoms is represented in the form

$$E = \frac{1}{2}\sum_{i\neq j}\phi_{ij}(r_{ij}),$$

where r_{ij} is the distance between atoms i and j and the bond energy ϕ_{ij} is taken as

$$\phi_{ij} = f_c(r_{ij})[A\exp(-\lambda_1 r_{ij}) - b_{ij}B\exp(-\lambda_2 r_{ij}) + c_0]. \quad (1)$$

Here, the bond order b_{ij} is given by

$$b_{ij} = \left(1 + \xi_{ij}^{\eta}\right)^{-\delta},$$

where

$$\xi_{ij} = \sum_{k \neq i,j} f_c(r_{ij}) g(\theta_{ijk}) \exp[\alpha(r_{ij} - r_{ik})^{\beta}].$$

The term $(1 + \xi_{ij})$ represent an effective coordination number of atom i and $f_c(r_{ij})$ is a cutoff function. The latter has the form

$$f_c(r) = \begin{cases} 1, & r \leqslant R_1 \\ \frac{1}{2} + \frac{9}{16}\cos\left(\pi \frac{r-R_1}{R_2-R_1}\right) - \frac{1}{16}\cos\left(3\pi \frac{r-R_1}{R_2-R_1}\right), & R_1 < r < R_2, \\ 0, & r \geqslant R_2, \end{cases}$$

where R_1 and R_2 are cutoff radii. The outer cutoff R_2 is chosen between the first and second coordination shells of the diamond cubic structure. The angular function $g(\theta_{ijk})$ has the generalized form

$$g(\theta) = c_1 + \frac{c_2(h - \cos\theta)^2}{c_3 + (h - \cos\theta)^2} \times \{1 + c_4 \exp[-c_5(h - \cos\theta)^2]\},$$

where θ_{ijk} is the angle between the bonds ij and ik. These functional forms are the same as for the MOD potential [7], except for the new coefficient c_0 that was added to better control the attractive part of the potential.

The adjustable parameters of the potential are A, B, α, h, η, λ_1, λ_2, R_1, R_2, δ, c_0, c_1, c_2, c_3, c_4, and c_5. The power β is a fixed odd integer. In the original Tersoff potential [2–4] $\beta = 3$, whereas Kumagai *et al.* [7] chose $\beta = 1$. We tried both numbers and found that $\beta = 3$ gives a better potential.

The free parameters of the potential were trained to reproduce basic physical properties of the diamond cubic (A4) structure and the energies of several alternate structures. Specifically, the fitting database included the experimental lattice parameter a, cohesive energy E_c, elastic constants c_{ij}, and the vacancy formation energy E_v^f. The alternate structures were simple cubic (SC), β-Sn (A5), face-centered cubic (FCC), hexagonal closed pack (HCP), body-centered cubic (BCC), simple hexagonal (HEX), wurtzite (B4), BC8, ST12, and clathrate (cP46). Their energies obtained by DFT calculations are available from open-access databases such as Materials Project [21], OQMD [22], and AFLOW [23,24]. Some of these structures were found experimentally as Si polymorphs under high pressure, others were only generated in the computer for testing purposes. The parameter optimization process utilized a simulated annealing algorithm. The objective function was the sum of weighted squares of deviations of properties from their target values. Numerous optimization runs were conducted using the weights as a tool to achieve the most meaningful distribution of the errors over different properties. Several versions of the potential were generated and the version deemed to be most reasonable was selected as final. This selection was somewhat subjective and was based on our ideas about how the potential will probably be used and which properties will matter most. Since it is impossible for this (or any other) potential to reproduce all properties with equal accuracy, priorities must be given to some properties over others. The present potential focuses on thermal and mechanical properties of bulk Si, especially at high temperatures.

The optimized potential parameters are listed in Table I. The potential has been incorporated in the molecular dynamics package LAMMPS (Large-scale Atomic/Molecular Massively Parallel Simulator) [25] as the pair style `tersoff/mod/c`.

The transferability of the new potential was evaluated by computing a number of physical properties that were not included in the training database and comparing the results with experimental data and/or DFT calculations available in the literature. The same comparison was made for the MOD, MEAM, and SW potentials to demonstrate their strengths and weaknesses relative to the new potential. We utilized the MOD and SW potential files from the LAMMPS potential library. The MEAM potential file was obtained from the developers [14]. The potential testing results are reported in the next section.

TABLE I. Optimized parameters of the new Si potential. Parameters of the MOD potential [7] are listed for comparison.

Parameter	Present	MOD[a]
A (eV)	3198.51383	3281.5905
B (eV)	117.780724	121.00047
λ_1 (Å^{-1})	3.18011795	3.2300135
λ_2 (Å^{-1})	1.39343356	1.3457970
η	2.16152496	1.0000000
$\eta \times \delta$	0.544097766	0.53298909
α	1.80536502	2.3890327
β	3	1
c_0 (eV)	−0.0059204	0.0
c_1	0.201232428	0.20173476
c_2	614230.043	730418.72
c_3	996439.097	1000000.0
c_4	3.33560562	1.0000000
c_5	25.2096377	26.000000
h	−0.381360867	−0.36500000
R_1 (Å)	2.54388270	2.7
R_2 (Å)	3.20569403	3.3

[a]Reference [7].

TABLE II. Properties of diamond cubic Si computed with four interatomic potentials in comparison with experimental data and DFT calculations.

Property	Experiment	DFT	Present	MOD[d]	MEAM[w]	SW[u]
E_c (eV/atom)	4.63[c]	4.84[r]	4.630	4.630	4.630	4.337
a (Å)	5.430[a]	5.451[r]	5.434	5.429	5.431	5.431
c_{11}(GPa)	165[a]; 167.40[b]		172.6	166.4	163.8	151.4
c_{12} (GPa)	64[a]; 65.23[b]		64.6	65.3	64.5	76.4
c_{44} (GPa)	79.2[a]; 79.57[b]		81.3	77.1	76.5	56.4
$\nu_{\max}$ (THz)	15.7[o]		17.6	17.5	25.6	17.8
Vacancy:						
E_v^f (T_d) (eV)	3.6[j]	3.17[m]; 3.69[t] 3.29–4.3[h]; 3.70 − 3.84[s]	3.54	2.82	3.57	2.64
E_v^f (D_{3d}) (eV)		3.97[t]; 4.29[v]; 4.37[n] 3.67 − 3.70[s]; 5.023[i]	3.61	–	3.77	–
Interstitials:						
E_i^f (hex) (eV)		3.31–5[h]; 2.87 − 3.80[s]	3.51	4.13[d]	–	–
E_i^f (T_d) (eV)		3.43–6[h]; 3.43 − 5.10[s]	3.01	3.27[d]	4.12	4.93
E_i^f (B) (eV)		4–5[h]	4.34	5.03[d]	6.78	5.61
E_i^f ⟨110⟩(eV)		3.31–3.84[h]; 2.87 − 3.84[s]	3.26	3.57[d]	3.91	4.41
Surface energy γ_s (J m^{-2}):						
{111}	1.24[q]; 1.23[p]	1.57[l]; 1.74[f]	1.11	0.89	1.2	1.36
{100}		2.14[l]; 2.39[f]; 2.36[k]	2.19	1.77	1.74[e]	2.36
$\{100\}_{2\times1}$	1.36[p]	1.71[g]; 1.45[f]; 1.51[k]	1.21	1.07	1.24	1.45
{110}	1.43[p]	1.75[k]	1.36	1.08	1.41	1.67
Melting:						
T_m(K)	1687		1687	1681[d]; 1682	1687[w]	1691[v]; 1677
$\Delta V_m/V_{\text{solid}}$ (%)	−5.1[a]		−3.8	−12.5	−2.7	−7.2
L (kJ/mol)	50.6[a]		24.0	34.7	43.2	31.1

[a]Reference [26].
[b]Reference [27].
[c]Reference [103].
[d]Reference [7].
[e]Constrained relaxation.
[f]Reference [43].
[g]Reference [104].
[h]References in Ref. [7].
[i]Reference [36].
[j]Reference [38].
[k]Reference [105].
[l]Reference [17].
[m]Reference [34].
[n]Reference [37].
[o]Reference [29].
[p]Reference [106].
[q]Reference [107].
[r]Reference [108].
[s]Reference [109].
[t]Reference [35].
[u]Reference [1].
[v]Reference [33].
[w]Reference [14].

III. PROPERTIES OF SOLID Si

Table II summarizes some of the properties of crystalline Si predicted by the four potentials. All properties have been computed in this work unless otherwise is indicated by citations. The defect energies are reported after full atomic relaxation.

A. Lattice properties

The present potential, MOD, and MEAM accurately reproduce the elastic constants. The SW potential gives less accurate elastic constants and a positive Cauchy pressure contrary to experiment [26,27]. The phonon density of states (DOS) and phonon dispersion relations were computed by the method

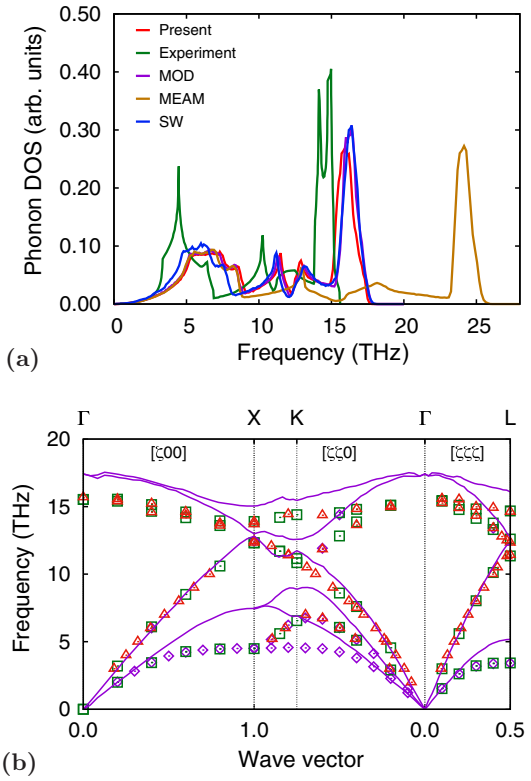

FIG. 1. Phonon properties of diamond cubic Si. (a) Density of states calculated with different interatomic potentials in comparison with experimental data [31]. (b) Dispersion relations at room temperature computed with the present potential in comparison with experiment: diamond symbols [30], squares [29], and triangles [32], respectively.

developed by Kong [28] and implemented in LAMMPS. The MD simulation was performed at 300 K utilizing a primitive $16 \times 16 \times 16$ supercell with 8192 atoms. The DOS plots are shown in Fig. 1(a) and the respective zone-center optical frequencies $\nu_{\max}$ are indicated in Table II. The present potential, MOD, and SW predict surprisingly similar $\nu_{\max}$ values that overestimate the experimental frequency by about 2 THz. The MEAM potential overshoots $\nu_{\max}$ by about 10 THz and the entire DOS is stretched by a factor of 1.63. Note that none of the four potentials reproduces the sharp peak at about 5 THz arising from the acoustic zone-boundary phonons.

Figure 1(b) displays the phonon dispersion curves predicted by the present potential. While general agreement with experiment [29–32] is evident and the longitudinal acoustic branches are reproduced accurately, the potential overestimates the transverse acoustic zone-boundary frequencies and the optical frequencies.

The cubic lattice parameter a was computed as a function of temperature by zero-pressure MD simulations. The linear thermal expansion coefficient $(a - a_0)/a_0$ relative to room temperature (a_0 at 295 K) is compared with experimental data in Fig. 2. The SW potential demonstrates exceptionally good agreement with experiment. The present potential slightly overestimates the experiment at temperatures below 1300 K and underestimates at higher temperatures. The negative slope at high temperatures is unphysical, but the overall agreement with experiment is reasonable. The slight negative slope is

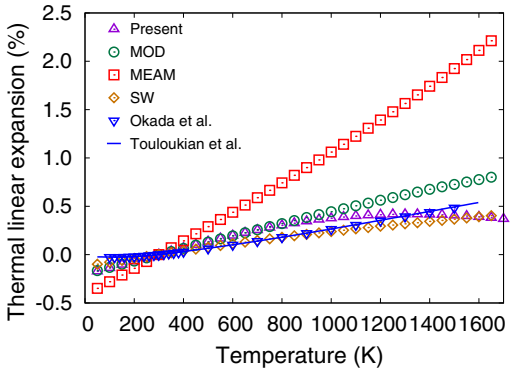

FIG. 2. Linear thermal expansion of Si lattice, $(a - a_0)/a_0$, relative to room temperature (a_0 at 295 K) predicted by four interatomic potentials in comparison with experimental measurements [122,123].

not a serious limitation to the use of this potential. Most thermodynamic properties depend primarily on the magnitude of the lattice constant at finite/high temperatures, not its temperature derivative. The MOD potential gives a similar thermal expansion at low temperatures but over-predicts it at high temperatures. The MEAM potential grossly overestimates the thermal expansion. Given also the poor agreement for phonons, care should be exercised when using this potential for thermodynamic calculations of crystalline Si. Note that neither phonon properties nor thermal expansion were included in the fitting databases of the potentials.

B. Lattice defects

According to DFT calculations [33–37], a Si vacancy can exist in several metastable structures. In the lowest-energy structure, the four neighbor atoms slightly move towards the vacant site preserving the tetrahedral (T_d) symmetry and leaving four dangling bonds. A slightly less favorable structure is obtained when one of the four atoms moves towards the other three and forms six identical bonds. This configuration has a hexagonal (D_{3d}) symmetry and is referred to as the "dimerized" or "split" vacancy. This vacancy reconstruction eliminates the dangling bonds but increases the elastic strain in the surrounding lattice. The present potential and MEAM correctly predict the split vacancy to be less stable than the T_d vacancy. The latter has the formation energy within the range of DFT calculations and consistent with the experimental value of 3.6 eV [38]. (It should be noted, though, that the experiments are performed at high temperatures at which the vacancy structure is unknown.) The MOD and SW potentials significantly under-predict the formation energy of the T_d vacancy. In addition, with the MOD potential the split vacancy spontaneously transforms to a D_{2d} structure with the energy of 3.41 eV (the DFT value is 3.46 eV) [39], whereas the SW potential predicts the split vacancy to be mechanically unstable and spontaneously transform to the T_d structure.

Self-interstitials can exist in four distinct configurations: hexagonal (hex), tetrahedral (T_d), bond center (B), and ⟨110⟩ split (Table II). Given the large scatter of the DFT formation energies, all four potentials perform almost equally well. There is one exception: the MEAM and SW potentials predict

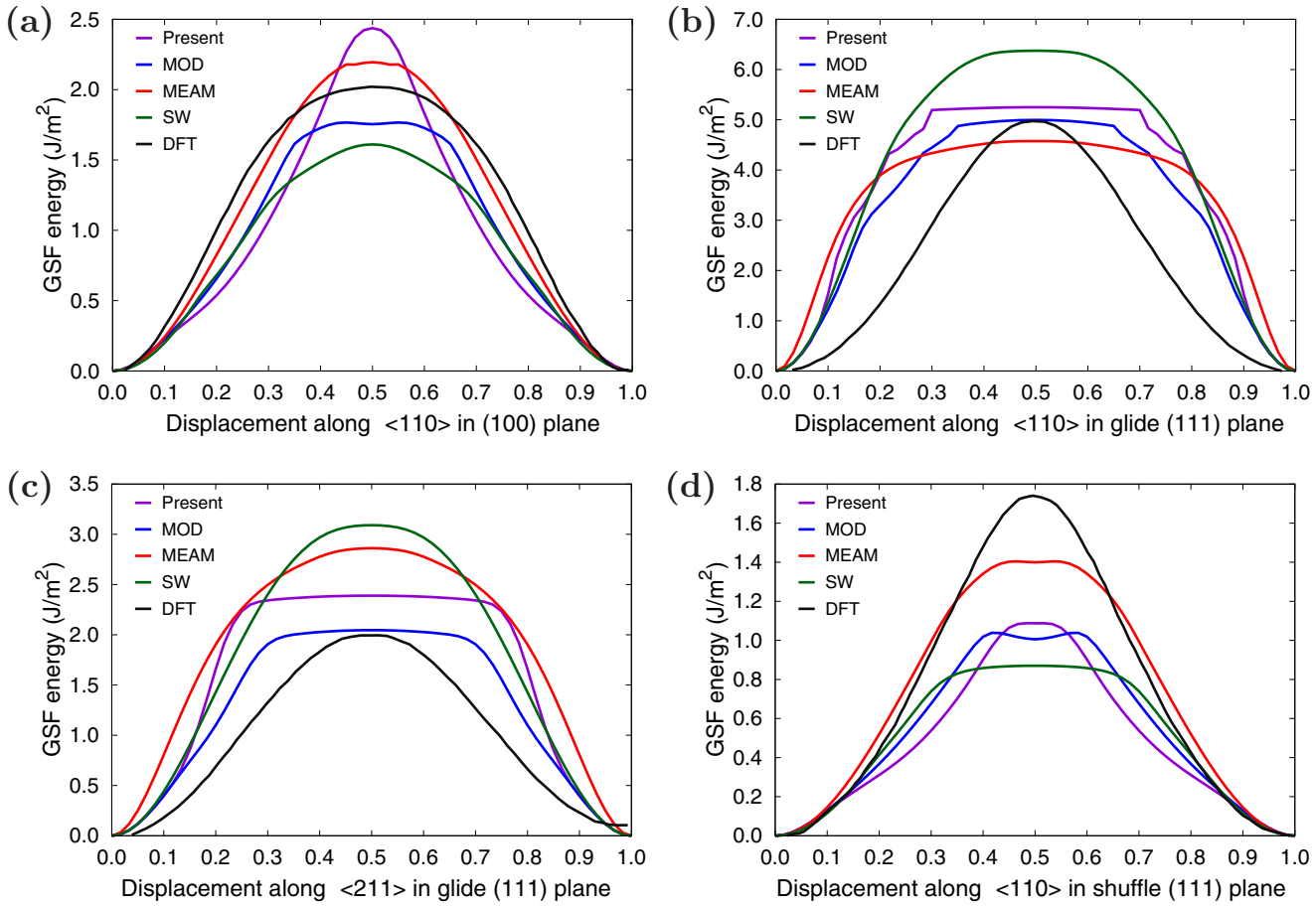

FIG. 3. Selected cross-sections of the {111} and {100} gamma surfaces predicted by the present potential in comparison with other potentials and DFT calculations [120,121].

the hexagonal interstitial to be mechanically unstable and spontaneously transform to the tetrahedral configuration. Both potentials overestimate the B-interstitial energy.

Surface energies were computed for the low-index orientations {100}, {110}, and {111}. Experiments have shown that these surfaces can undergo reconstructions to several different structures [40–42]. Reconstructions of the {110} and {111} surfaces are accompanied by a modest energy reduction of about 0.3–0.4 J m^{-2}. In this paper, these surfaces were tested in unreconstructed states. By contrast, the dimer reconstruction of the {100} surface to the more stable 2 × 1 structure reduces the surface energy by almost 1 J m^{-2}. In this case, both reconstructed and unreconstructed structures were compared with DFT calculations. Table II shows that the SW potential does an excellent job reproducing the DFT surface energies. The MOD potential is the least accurate: it systematically underestimates the surfaces energies for all orientations. The present potential demonstrates a substantial improvement over MOD: all energies are higher and closer to the DFT data. The MEAM potential is equally good for all surfaces except for the unreconstructed {100} structure. The latter is mechanically unstable with this potential and reconstructs to the 2 × 1 structure spontaneously during static relaxation at 0 K. This instability was not observed in the DFT calculations [43]. The surface energy of 1.74 J m^{-2} shown in the table was obtained by constrained relaxation of this surface, in which the atoms were only allowed to move in the direction normal to the surface to prevent the dimerization. With the potential proposed in this work, the unreconstructed {100} surface is stable at 0 K and forms symmetrical rows of dimers corresponding to the 2 × 1 reconstruction upon heating to 1000 K and slowly cooling down to 0 K.

As another test of the potentials, unstable stacking fault energies γ_{us} were calculated for the {111} and {100} crystal planes. Such faults are important for the description of dislocation core structures. In silicon, dislocations glide predominantly on {111} planes. The spacing between {111} planes alternates between wide and narrow. In the former case the chemical bonds are normal to the planes while in the latter they are at 19.47° angles. A generalized stacking fault is obtained by translation of one half-crystal relative to the other in a chosen direction parallel to a {111} plane. Depending on whether the cutting plane passes between widely spaced or narrowly spaced atomic layers, the stacking fault is called shuffle type or glide type, respectively. After each increment of crystal translation, the atoms are allowed to minimize the total energy by local displacements normal (but no parallel) to the fault plane. The excess energy per unit surface area plotted as a function of the translation vector is called the gamma-surface. If the dislocation Burgers vector is parallel to a crystallographic direction ⟨*hkl*⟩, then its core structure is dictated by the {111}⟨*hkl*⟩ cross-sections of the gamma

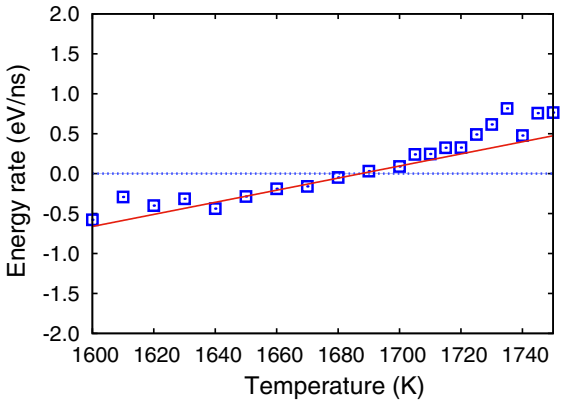

FIG. 4. Rate of energy change as a function of temperature during melting and crystallization of Si modeled with the present potential. The line is the linear fit to determine the melting temperature.

surface. The unstable stacking fault energy γ_{us} is the maximum energy in this cross-section.

Figure 3 displays three cross-sections of the $\{111\}$ gamma surface computed with the four potentials in comparison with DFT calculations. The figure additionally includes the $\{100\}\langle 110\rangle$ cross-section for which DFT data is available. The respective γ_{us} values are summarized in Table V. While none of the potentials reproduces the DFT curves well, the SW potential tends to be the least accurate. For some of the cross-sections, the Tersoff-type potentials "chop off" the tip of the curve due to the short range of atomic interactions and a relatively sharp cutoff. It should also be noted that the potentials do not reproduce the stable stacking fault predicted by DFT calculations [Fig. 3(c)]. This fault arises due to long-range interactions and is not captured by these potentials.

IV. MELTING TEMPERATURE AND LIQUID PROPERTIES OF SI

The melting temperature was computed by the interface velocity method. A periodic simulation block containing a (111) solid-liquid interface was subject to a series of isothermal MD simulations in the NPT ensemble (zero pressures in all directions) at several different temperatures. The interface migrated towards one phase or the other, depending on whether the temperature was above or below the melting point. The total energy of the system was monitored in this process and was found to be a nearly linear function of time. The slope of this function gives the rate of the energy change due to the phase transformation. A plot of this energy rate as a function of temperature was used to find the melting point by linear interpolation to the zero rate (Fig. 4). For the present potential, the melting temperature obtained was found to be $T_m = 1687 \pm 4$ K (the error bar is the standard deviation of the linear fit). This temperature is in excellent agreement with the experimental melting point of 1687 K, even though it was not included in the fitting procedure.

To verify our methodology, similar calculations were performed for the MOD potential. The result was $T_m = 1682 \pm 4$ K, which matches 1681 K reported by the potential developers [7]. For the SW potential, the same method gives

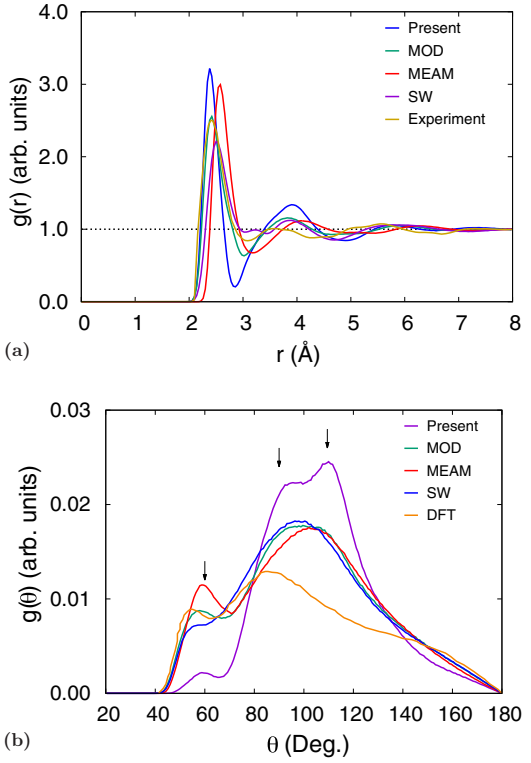

FIG. 5. Structure of liquid Si: (a) pair correlation function $g(r)$ and (b) bond-angle distribution $g(\theta,r)$ computed with the present interatomic potential at the temperature of 1750 K in comparison with the first-principles calculation at 1767 K [50], experimental data at 1733 K [47], and the MOD, MEAM, and SW potentials at 1767 K. The arrows indicate the angles of 60°, 90°, and 109.47°.

$T_m = 1677 \pm 4$ K. This number is consistent (within the error bars) with $T_m = 1691 \pm 20$ K obtained by thermodynamic calculations [44]. The energy rate versus temperature plots for the MOD and SW potentials can be found in the Supplemental Material to this paper [45].

Table II summarizes the predictions of the four potentials for the latent heat of melting L and the volume effect of melting ΔV_m relative to the volume of the solid V_{solid}. None of the potentials reproduces these properties well. The present potential gives the most accurate volume effect $\Delta V_m / V_{\text{solid}}$ but the least accurate latent heat L. The MOD potential predicts a better value of L but overestimated the volume effect a factor of two.

Prediction of structural properties of liquid Si presents a significant challenge to interatomic potentials. The nature of atomic bonding in Si changes from covalent to metallic upon melting [46], causing an increase in density. In this work, the structure of liquid Si was characterized by the pair correlation function $g(r)$ and the bond-angle distribution function $g(\theta,r)$. These functions were averaged over 300 uncorrelated snapshots from NPT MD simulations under zero pressure at 1750 K using a simulation block containing 6912 atoms. The angular distribution $g(\theta,r)$ was computed for bonds within the radius r_m of the first minimum of $g(r)$ and normalized by unit area under the curve. The coordination number N_c was computed using the same radius r_m.

TABLE III. Energies (eV/atom) of alternate crystal structures of Si relative to the cubic diamond phase in comparison with first-principles calculations.

Structure	*Ab initio*	Present	MOD[i]	MEAM[l]	SW[a]
FCC	0.449[c]; 0.57[f]; 0.537[h],[m] 0.6494[n]; 0.5536[p]	1.113	0.4473	0.8975	0.3963
HCP	0.55[f]; 0.508[m]; 0.5946[n]; 0.5301[p]	1.1019	0.4426	0.8909	0.3963
BCC	0.43[q]; 0.435[c]; 0.46[j]; 0.53[f]; 0.523[m]; 0.6142[p]	0.6945	0.4377	0.5354	0.2810
HEX	0.293[e]	0.7322	0.3901	0.5591	0.3876
SC	0.276[c]; 0.35[f]; 0.38[b]	0.2849	0.3076	0.4688	0.2745
β-Sn	0.19[d]; 0.33[d]; 0.414[d]; 0.454[d] 0.3264[n]; 0.27[f]; 0.32[b]; 0.290[h] 0.2718[p]; 0.380[r]; 0.291[m]	0.3725	0.3343	0.3671	0.2012
BC8	0.13[s]; 0.159[h]; 0.126[j] 0.110[k]; 0.166[n]	0.2008	0.2127	0.2502	0.1880
Wurtzite	0.011[h],[m]; 0.016[f]	0.0000	0.0000	0.00001	0.0000
ST12	0.136[j]; 0.1181[k]	0.3900	0.4470	0.6031	0.4857
cP46	0.063[h]; 0.0637[n]	0.0703	0.0581	0.0625	0.0502
h-Si_6	0.35[g]	0.5021	0.5863	0.6464	0.8417
Si_{24}	0.09[t]	0.1816	0.1864	0.2340	0.1949
RMS error		0.2883	0.1124	0.2138	0.1745

[a]Reference [1].
[b]Reference [104] and references therein.
[c]Reference [7].
[d]Reference [110] and references therein.
[e]Reference [111] and references therein.
[f]Reference [108].
[g]Reference [51].
[h]Reference [21].
[i]Reference [7].
[j]Reference [112].
[k]Reference [113].
[l]Reference [14].
[m]Reference [22].
[n]Reference [114].
[p]References [23,24].
[q]Reference [115].
[r]Reference [116].
[s]Reference [117].
[t]Reference [52].

The results are shown in Fig. 5. The present potential turns out to be the least accurate for the liquid properties. The first maximum of $g(r)$ is too high and the first minimum too deep in comparison with experiment [47]. The other potentials perform better but still show significant departures from the experiment. The MOD potential gives the coordination number $N_c \approx 5.7$ in closest agreement with the experimental value $N_c \approx 6.4$ [48], whereas the present potential and the MEAM potential give $N_c \approx 4.3$ and $N_c \approx 4.2$, respectively. For the bond-angle distribution, the results computed with the four potentials are very different and none agrees with the DFT simulations. The DFT simulations (*ab initio* MD)[49,50] yield a broader distribution with two peaks of comparable height centered at 60° and 90°. The present potential strongly underestimates the 60° peak, overestimates the peak at 90°, and creates another peak at the tetrahedral angle of 109.47°. Using the other potentials, the position of the large peak varies between 90° and 109.47°. Overall, our potential overestimates the degree of structural order in the liquid phase.

V. ALTERNATE CRYSTAL STRUCTURES OF SI

Tables III and IV show the equilibrium energies of several crystal structures of Si relative to the diamond cubic structure and the respective equilibrium atomic volumes. All these structures were included in the potential fitting procedure except for two. The h-Si_6 structure was recently found by DFT calculations as a new mechanically stable polymorph of Si attractive for optoelectric applications due to its direct band gap of 0.61 eV and interesting transport and optical properties [51]. The h-Si_6 structure is composed of Si triangles forming a hexagonal unit cell with the $P6_3/mmc$ space group. Si_{24} is another mechanically stable polymorph that has recently been synthesized by removing Na from the Na_4Si_{24} precursor [52]. The orthorhombic $Cmcm$ structure of Si_{24} contains open channels composed of six and eight-member rings. This polymorph has a quasidirect 1.3 eV band gap and demonstrates unique electronic and optical properties making it a promising candidate for photovoltaic and other applications. The h-

TABLE IV. Equilibrium volume per atom (Å^3) of alternate crystal structures of Si in comparison with experiment and first-principles calculations.

Structure	Experiment	*Ab initio*	Present	MOD[e]	MEAM[h]	SW[a]
Diamond	20.024[f]	20.264[c]; 20.444[d]; 20.439[i]; 20.33[b,l]; 19.59[l]; 20.46[m]; 19.03[g]; 16.686[f]; 20.385[j] 19.77[b]; 20.42[b]; 20.124[b]; 20.21[b]; 20.08[b]	20.052	20.002	20.024	20.023
FCC		14.678[c]; 14.484[d]; 14.504[i]; 14.810[j]; 14.337[k]	14.448	14.262	17.312	17.824
HCP		14.477[c]; 14.313[i]; 14.68[j]	14.439	14.257	17.279	17.824
BCC		14.738[c]; 14.2427[k]	14.483	14.045	15.592	17.082
HEX		15.21[l]; 14.56[l]; 13.15[p]	15.423	14.992	17.457	18.230
SC		16.179[c]; 15.7653[k]	15.639	15.581	18.194	17.822
β-Sn	14.0[f]; 14.2[f]	15.479[c]; 15.334[d]; 16.0[f]; 15.292[i] 14.92[b]; 15.45[b]; 15.25[b]; 15.34[b] 15.31[b]; 15.405[j]; 15.35[m]; 14.8859[k]	15.016	15.085	16.560	17.275
BC8	18.13[f]; 18.26[f]	17.724[f]; 17.48[g]; 18.44[j]; 18.427[d] 18.2619[k]; 18.082[n]	18.112	18.079	19.374	17.902
Wurtzite		20.324[c]; 20.440[d]; 20.380[i]; 19.7575[k]	20.052	20.002	20.024	20.023
ST12		17.65[g]; 17.57[g]	18.083	18.123	20.931	18.325
cP46		23.256[d]; 23.214[i]; 23.128[j]	22.746	22.663	23.042	22.663
h-Si_6		27.188[q]	28.575	28.725	33.460	31.667
Si_{24}	21.52[r]	21.934[r]	21.861	21.809	23.189	22.083
RMS error			0.6758	0.6609	1.9147	2.0452

[a]Reference [1].
[b]Reference [110] and references therein.
[c]Reference [108].
[d]Reference [21].
[e]Reference [7].
[f]Reference [112] and references therein.
[g]Reference [113].
[h]Reference [14].
[i]Reference [22].
[j]Reference [114].
[k]Reference [20].
[l]Reference [118].
[m]Reference [116].
[n]Reference [119].
[p]Reference [111].
[q]Reference [51].
[r]Reference [52].

Si_6 and Si_{24} structures were used for testing purposes to evaluate the transferability of the potentials. All structures were equilibrated by isotropic volume relaxation without local displacements of atoms. For the HCP and wurtzite structures, the c/a ratios were fixed at the ideal values. For the simple hexagonal, β-Sn and h-Si_6 structures, c/a was fixed at the DFT values of 0.94, 0.552, and 0.562, respectively. It is worth mentioning that the present potential and MOD predict the wurtzite phase to be mechanically unstable at 0 K, which appears to be a generic feature of Tersoff-type potentials.

TABLE V. Energies γ_{us} (in J m^{-2}) of unstable stacking faults computed with the present interatomic potential in comparison with other potentials and first-principles calculations.

Property	*Ab initio*	Present	MOD[a]	MEAM[b]	SW[c]
(111)⟨110⟩ shuffle	1.81[d,e]	1.09	1.04	1.40	0.87
(111)⟨110⟩ glide	4.97[f]	5.25	5.00	4.58	6.37
(111)⟨211⟩ glide	2.02[d,e]	2.39	2.05	2.86	3.09
(100)⟨110⟩	2.15[e]	2.44	1.77	2.19	1.61

[a]Reference [7].
[b]Reference [14].
[c]Reference [1].
[d]Reference [120].
[e]Reference [121].
[f]Digitized from Ref. [121].

In Tables III and IV, we compare the predictions of the four potentials with DFT calculations available in the literature. Since the tables are overloaded with numerical data, we found it instructive to recast this information in a graphical format. In Figs. 6 and 7, we plot the energies (volumes) predicted by each potential against the respective DFT energies (volumes) computed by different authors. The bisecting line is the line of perfect correlation. The first thing to notice is the large scatter of the DFT data reported by different sources, which makes a comparison with potentials somewhat ambiguous. For each potential, the agreement was quantified by the root-mean-square (RMS) deviation of the data points from

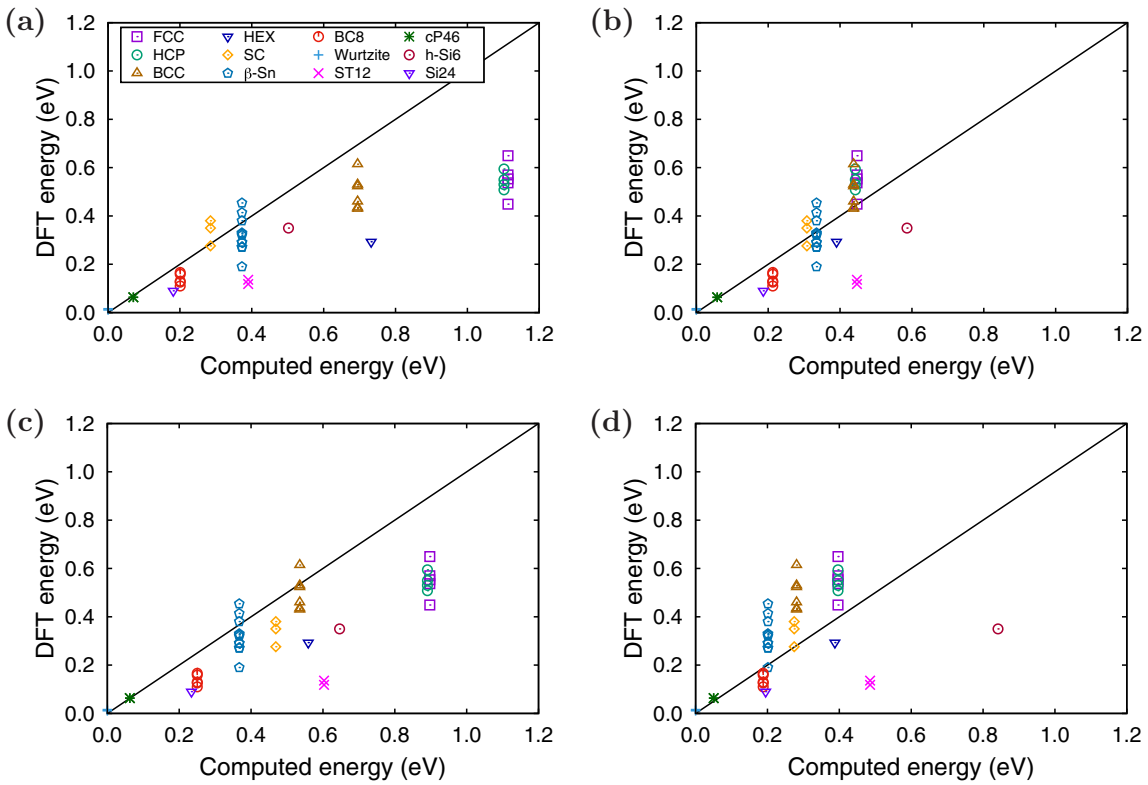

FIG. 6. DFT energies of crystal structures of Si vs the energies predicted by interatomic potentials: (a) present potential, (b) MOD potential [7], (c) MEAM potential [14], and (d) SW potential [1]. The energies are counted per atom relative to the diamond cubic structure. The line of perfect correlation is indicated.

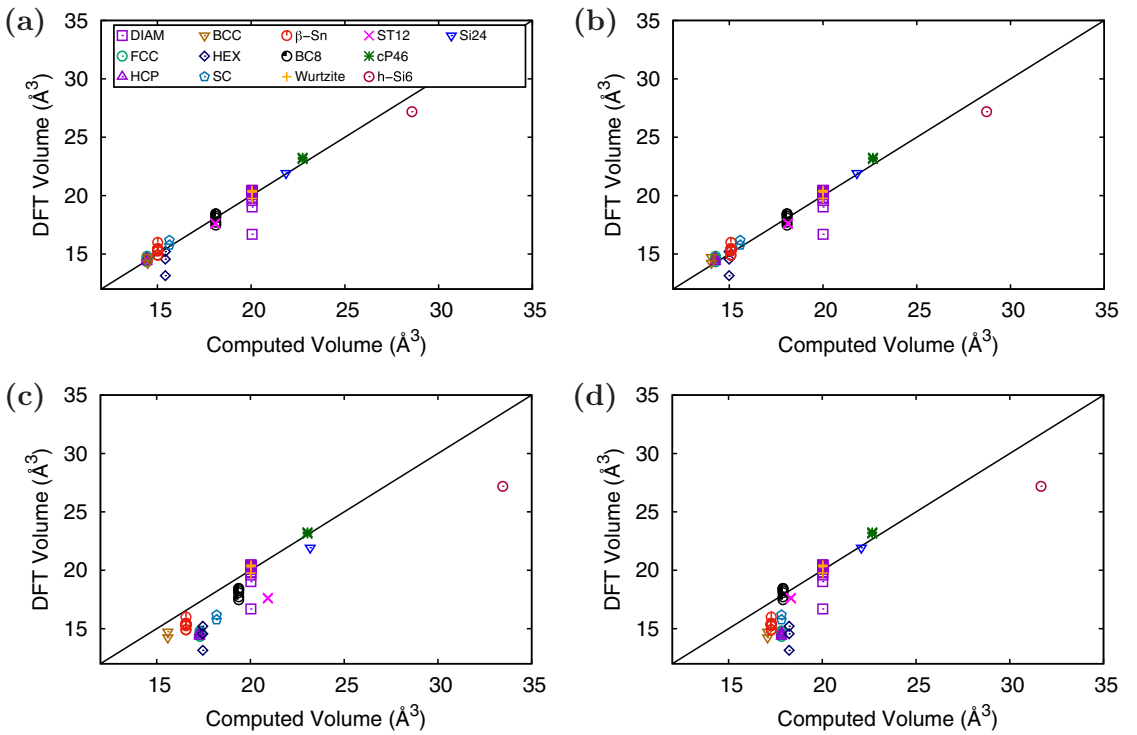

FIG. 7. DFT atomic volumes of crystal structures of Si vs the atomic volumes predicted by interatomic potentials: (a) present potential, (b) MOD potential, [7], (c) MEAM potential [14], and (d) SW potential [1]. The line of perfect correlation is indicated.

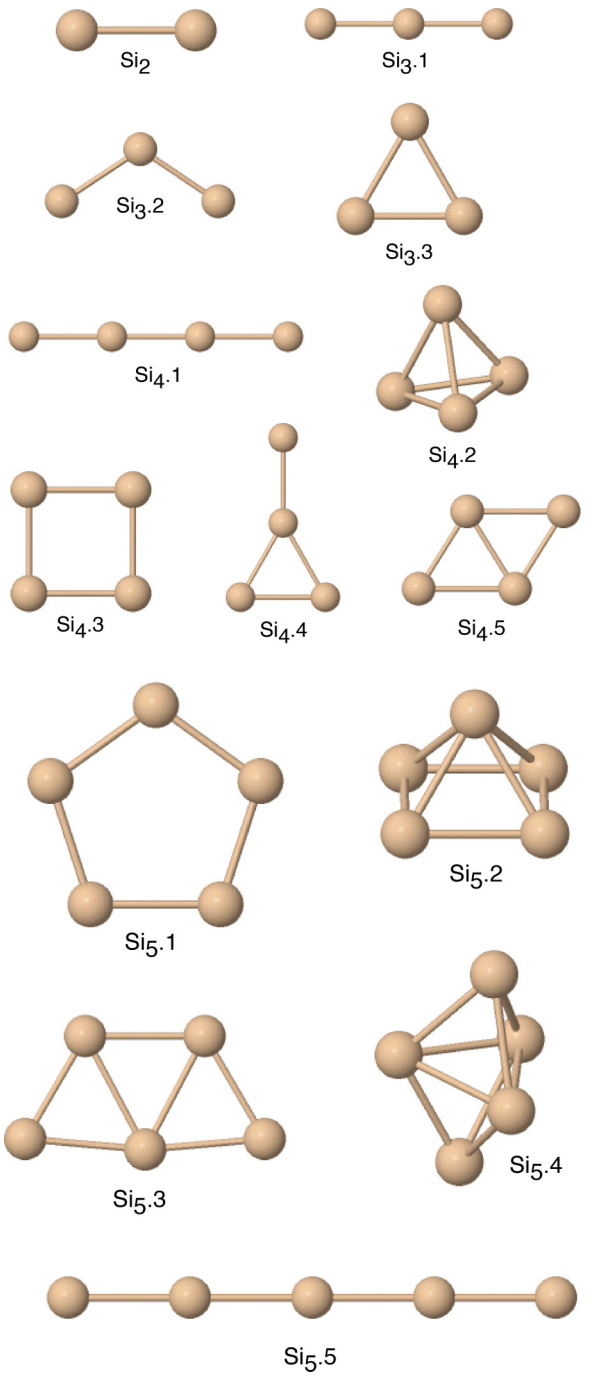

FIG. 8. Structures of dimer, trimer, tetramer, and pentamer Si clusters tested in this work. The labels indicate the cluster notations.

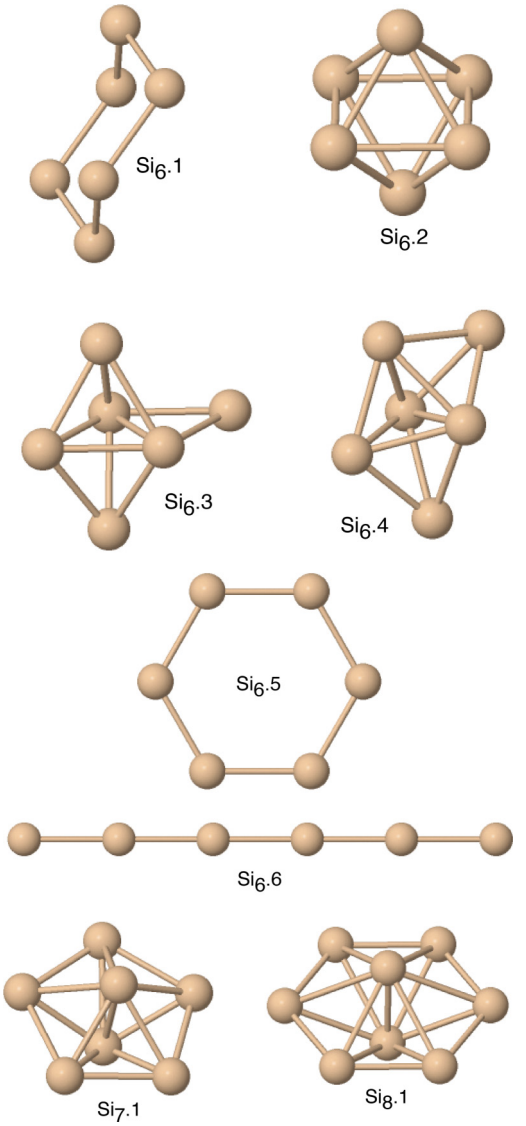

FIG. 9. Structures of hexamer, heptamer, and octamer Si clusters tested in this work. The labels indicate the cluster notations.

the bisecting line. The RMS deviations obtained are shown in the last row of Tables III and IV. It should emphasized that these RMS deviations reflect not only the differences between the potentials and the DFT calculations but also the scatter of the DFT points themselves. Thus only comparison of relative values of the RMS deviations makes sense. It should also be noted that the energy deviations are strongly dominated by high-energy structures, such as the close-packed FCC and HCP phases. With this in mind, it is evident that the present potential is the least successful in reproducing the structural energies, whereas the MOD potential is the most successful. For the atomic volumes, however, the present potential and MOD are equally accurate, while the SW and MEAM potentials show significantly larger deviations.

It is interesting to note that the present potential gives the most accurate predictions for the energy and volume of the novel h-Si_6 and Si_{24} structures that were not included in the fitting database. The MOD potential comes close second, whereas the MEAM and SW potentials are significantly less accurate. The energy-volume plots for several selected structures can be found in Ref. [45].

VI. SILICON CLUSTERS

Structure and properties of small Si clusters offer a stringent test of interatomic potentials. Potentials are usually optimized for bulk properties, whereas the clusters display very different and much more open environments in which the coordination number and the type of bounding may change very significantly from one structure to another. Si potentials are traditionally considered to be incapable of reproducing cluster

TABLE VI. Cohesive energies (eV/atom) of Si clusters relative to isolated atoms computed with four interatomic potentials in comparison with first-principles calculations. The asterisk marks mechanically unstable structures whose energies were obtained by anisotropic volume relaxation without local atomic displacements.

Cluster	Experiment	*Ab initio*	Present	MOD[a]	MEAM[b]	SW[c]
Si_2	1.62[d]	1.53[d]; 1.81[e]	1.327	1.788	2.473	1.084
Si_3.1		2.03[d]; 2.41[e]	1.710	2.003	2.519	1.267
Si_3.2	2.6[d]	2.39[d]; 2.58[e]	1.757	2.197	2.672	1.446
Si_3.3		2.61[e]	2.259	2.147	2.815	1.480
Si_4.1		1.82[d]; 2.48[e]	1.901	2.121	2.593	1.372
Si_4.2		2.02[d]; 2.49[e]	2.457	2.325*	2.984	1.669*
Si_4.3		2.21[d]; 2.73[e]	2.571	2.810	3.021	2.035
Si_4.4		2.22[d]	2.219	2.232	2.759	1.525
Si_4.5		2.68[d]; 3.09[e]	2.579	2.441*	2.995	1.746*
Si_5.1		2.02[d]; 2.62[e]	2.613	3.013	3.075	2.168
Si_5.2		2.69[d]; 3.04[e]	2.800	2.731	3.159	2.062
Si_5.3		3.09[e]	2.678	2.549*	3.037	1.845*
Si_5.4		2.78[d]; 3.30[e]	2.836	2.821	3.124	2.146
Si_5.5			2.017	2.192	2.626	1.433
Si_6.1		2.22[d]	2.618	3.023	3.075	2.168
Si_6.2		3.33[e]	2.862	2.793	3.269	2.142
Si_6.3		3.04[d]; 3.448[e]	2.664*	2.658*	3.225	1.970*
Si_6.4		3.453[e]	2.706*	2.771*	3.260	2.139*
Si_6.5			2.606	2.975	3.045	2.132
Si_6.6			2.093	2.239	2.651	1.475
Si_7.1		3.56[e]	2.938	2.960	3.344	2.321*
Si_8.1		3.22[e]	2.919	3.006*	3.267	2.379*
Chain		2.260[a]	2.477	2.475	2.771	1.680

[a]Reference [7].
[b]Reference [14].
[c]Reference [1].
[d]Reference [55] and references therein.
[e]Reference [54].

properties, unless such properties are specifically included in the fitting process as in the case of the Boulding and Andersen potential [53]. It was thus interesting to compare the predictions of the four potentials with first-principles calculations.

Figures 8 and 9 show the structures of the Si_n ($n = 2 - 8$) clusters tested in this work. Several different structures are included for each cluster size n whenever first-principles data is available. Such structures are labeled by index m in the $Si_n.m$ format in the order of increasing cohesive (binding) energy according to the DFT calculations [54]. Thus the structure labeled Si_n.1 represents the DFT-predicted ground state for each cluster size n (except for the dimer Si_2 that has a single structure). In addition to the DFT calculations [54], we included the results of quantum-chemical (QC) calculations on the Hartree-Fock level [55]. Such calculations are more accurate but the energy scale is not fully compatible with that of the DFT calculations. To enable comparison, we followed the proposal [56,57] that the QC energies be scaled by a factor of 1.2 to ensure agreement with experiment for the dimer energy.

Table VI summarizes the predictions of the four potentials in comparison with DFT calculations [54] and unscaled QC energies [55]. In addition to the clusters, we included an infinitely long linear chain for the sake of comparison. To aid visual comparison, Fig. 10 shows the cluster energies grouped by the cluster size (same-size clusters are connected by straight lines). The QC energies are plotted in the scaled format. Note that the scaling does indeed bring the QC and DFT energies to general agreement with each other. Despite the significant scatter of the individual energies on the level of 0.2–0.4 eV/atom, both calculation methods predict the same ground state for trimers, tetramers, and pentamers. None of the potentials predicts the correct ordering for all DFT/QC energies. The present potential and MOD show about the same level of accuracy, but the present potential makes less mistakes in the ordering. Both potentials tend to slightly under-bind the clusters. The MEAM potential is the most successful in reproducing the cluster energies, except for the dimer energy for which it is least accurate. There are mistakes in the ordering, but overall the deviations from the first-principles calculations are about the same as the difference between the two first-principles methods. The SW potential performs poorly: for some of the clusters, the binding energy is underestimated by more than 1 eV per atom. For the infinite atomic chain, the present potential and MOD are in closest agreement with the DFT/QC energies (Table VI). This comparison leads to the conclusion that, at least for the cluster structures tested here, the present potential, MOD and MEAM are quite capable of predicting the general trends of the cluster energies with a reasonable accuracy without fitting.

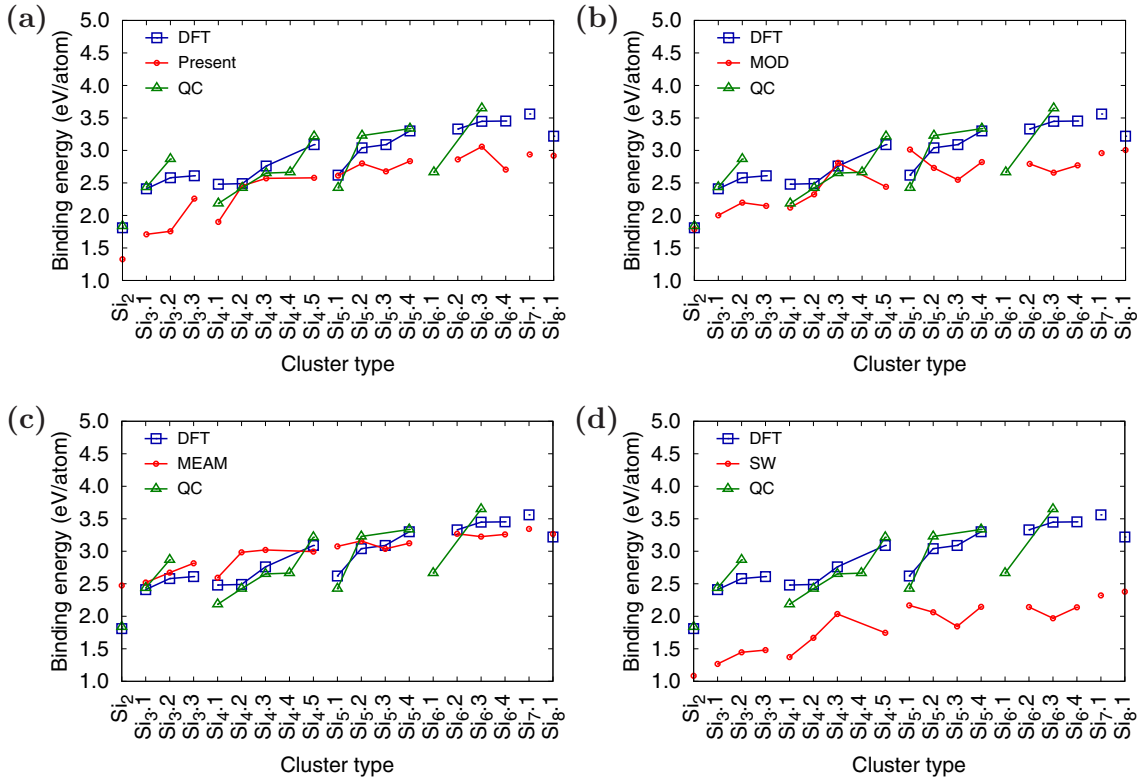

FIG. 10. Binding energies of Si clusters predicted by interatomic potentials: (a) present potential, (b) MOD potential [7], (c) MEAM potential [14], and (d) SW potential [1]. First-principles energies computed by DFT and QC methods are shown for comparison. The clusters are divided into groups corresponding to the same number of atoms and are ordered with increasing binding energy. The cluster structures are shown in Figs. 8 and 9.

VII. 2D SILICON STRUCTURES

A. Single-layer silicenes

Silicenes are 2D allotropes of Si that have recently attracted much attention due to their interesting physical properties and potential device applications [58–62]. By contrast to carbon, the sp^3 hybridized Si would seem to be an unlikely candidate for a 2D material. Nevertheless, epitaxial honeycomb Si layers have been found experimentally on metallic substrates such as (111)Ag [58–60,63–70]. DFT calculations also indicate that silicene can be stabilized by bilayer graphene [71,72]. Unlike in graphene, some of the 2D forms of Si can have a band gap and could be incorporated in Si-based microelectronics. In particular, electric field applied to the buckled honeycomb structure of silicene, which is normally semimetallic, can open a band gap whose magnitude increases with the field. It was predicted [73], and recently demonstrated [74] that single-layer silicene can work as a field-effect transistor [73]. Experimentally, it has not been possible so far to isolate free-standing silicenes. They are presently considered hypothetic 2D materials and have only been studied by DFT calculations. Such calculations predict that single-layer silicene can possess remarkable electric, optical and magnetic properties [75–78], in addition to ultra-low thermal conductivity [79].

The planar (graphenelike) silicene [Fig. 11(a)] is mechanically unstable and spontaneously transforms to the more stable buckled structure [Figs. 11(b) and 11(c)] [80–82]. The latter has a split width Δ of about 0.45–0.49 Å and a first-neighbor distance r_1 slightly different from that in the planar structure [73,80,82–85]. Furthermore, adsorption of Si ad-atoms on the buckled silicene creates a series of periodic dumbbell structures that are even more stable [79,81,84]. An adatom pushes a nearby Si atom out of its regular position and the two atoms form a dumbbell aligned perpendicular to the silicene plane. The dumbbell atoms have a fourfold coordination (counting the dumbbell bond itself) consistent with the sp^3 bonding. One of the best studied dumbbell silicenes has the $\sqrt{3} \times \sqrt{3}$ structure shown in Figs. 11(d)–11(f) (the dumbbell atoms are shown in blue and green). The dumbbells distort the hexagonal structural units and create three slightly different nearest-neighbor distances: $r_{\mathrm{I,II}}$, $r_{\mathrm{II,III}}$, and $\Delta_{\mathrm{III,III}}$ [Fig. 11(f)].

The energies and geometric characteristics of the three silicene structures predicted by the four potentials are listed in Table VII. The results of DFT calculations reported in the literature are included for comparison. The agreement with the DFT data is reasonable, especially considering that the 2D structures were not included in the fitting datasets of the potentials. The present potential, MOD, and MEAM demonstrate about the same agreement with the DFT calculations. The SW potential tends to be less accurate. For the planar structure, the MOD potential is the most accurate, followed by the present potential, MEAM, and then SW. All four potentials correctly predict that the planar structure is mechanically unstable and transforms to the buckled structure.

TABLE VII. Properties of single-layer silicenes computed with four interatomic potentials in comparison with DFT calculations.

Property	*Ab initio*	Present	MOD[a]	MEAM[b]	SW[c]
Honeycomb planar:					
E_c (eV/atom)	3.96[f]	3.6955	3.8280	3.6234	3.1450
b (Å)	3.895[f]	4.042	4.019	4.306	4.104
r_1 (Å)	2.249[f]	2.332	2.321	2.486	2.369
Honeycomb buckled:					
$\Delta E_c^{\text{buckled-diamond}}$ (eV/atom)	0.76[e]	0.88	0.69	0.89	1.09
$\Delta E_c^{\text{buckled-}\sqrt{3}\times\sqrt{3}}$ (eV/atom)	0.048[d]	0.14	−0.08	0.08	0.07
b (Å)	3.88[k]; 3.87[d,g]; 3.83[e]	3.870	3.820	3.944	3.840
r_1 (Å)	2.28[d]; 2.25[e,l]	2.328	2.312	2.449	2.352
Δ (Å)	0.44[d,e]; 0.45[g,j] 0.46[i]; 0.49[l]	0.655	0.694	0.901	0.784
$\sqrt{3}\times\sqrt{3}$ dumbbell:					
b (Å)	6.52[d,h]	6.475	6.471	6.312	6.604
$r_{\text{II,III}}$ (Å)	2.40[d,h]	2.393	2.425	2.526	2.513
$r_{\text{I,II}}$ (Å)	2.28[d]	2.333	2.425	2.456	2.359
$\Delta_{\text{III,III}}$ (Å)	2.76[h]	3.0564	3.111	3.160	3.261

[a]Reference [7].
[b]Reference [14].
[c]Reference [1].
[d]Reference [84].
[e]Reference [80].
[f]Reference [111].
[g]Reference [85].
[h]Reference [81].
[i]Reference [73].
[j]Reference [82].
[k]Reference [59].
[l]Reference [83].

The present potential, MEAM, and SW correctly predict that the $\sqrt{3}\times\sqrt{3}$ dumbbell structure has a lower energy than the buckled structure. By contrast, the MOD potential predicts that the $\sqrt{3}\times\sqrt{3}$ dumbbell structure has a higher energy, which is contrary to the DFT calculations. All four potentials overestimate the split width Δ in the buckled structure and the distance $\Delta_{\text{III,III}}$ between the dumbbell atoms in the $\sqrt{3}\times\sqrt{3}$ structure, the present potential being closest to the DFT data.

Ab initio MD simulations have shown that buckled silicene containing Stone-Wales defects remained stable (both free-standing and supported by a Ag substrate) for a period of 2 ps at 500 K [86]. Furthermore, according to MD simulations using a ReaxFF potential, free-standing buckled silicene survives a rapid temperature rise up to 2000 K in 500 ps [87]. We note that in both cases, the silicene sheet was subject to periodic boundary conditions in both directions parallel to its plane. In this work, the thermal stability of single-layer silicenes was evaluated by MD simulations on longer time scales. The simulated systems were subject to periodic boundary conditions at zero pressure. However, at least two dimensions of the simulation block were larger than the system size. For the nanoribbon and nanosheet, this simulation setup is less restrictive than in Refs. [86,87] and captures the destabilizing effect of the sheet edges.

Figure 12 demonstrates that a nanoribbon of buckled silicene is unstable at finite temperatures and quickly collapses to a cluster before temperature reaches 300 K. Likewise, a free-standing sheet (flake) of buckled silicene (Fig. 13) collapses into a cluster with the shape of a bowl when temperature reaches 300 K. The nanoribbon and nanoflake made of the $\sqrt{3}\times\sqrt{3}$ dimerized silicene collapse as well.

A single-wall nanotube was also tested for thermal stability. The latter was obtained by wrapping a layer planar silicene into a tube 49 Å in diameter (Fig. 14). The period along the tube axis was 122 Å. As soon as temperature began to increase starting from 0 K, the wall of the tube transformed to the buckled structure and then collapsed before the temperature reached 300 K. Qualitatively, the same behavior of the single-layer silicene structures was found with all four potentials. In all cases, the single-layer silicene easily developed waves due to thermal fluctuations until neighboring surface regions came close enough to each other to form covalent bonds. Once this happened, the bond-forming process quickly spread over the entire surface and the structure collapsed. This chemical reactivity and the lack of bending rigidity are the main factors that cause the instability of free-standing single-layer silicenes at room temperature.

B. Bilayer silicenes

Another interesting 2D form of silicon is the bilayer silicene [69,76,88–92]. Like the single-layer silicene discussed above, the bilayer silicene was found experimentally on top of metallic surfaces such as Ag(111) [69,88,90,92]. By contrast to bilayer graphene, the interlayer bonds in bilayer silicene are covalent sp^3 type. As a result, the formation of a bilayer is accompanied

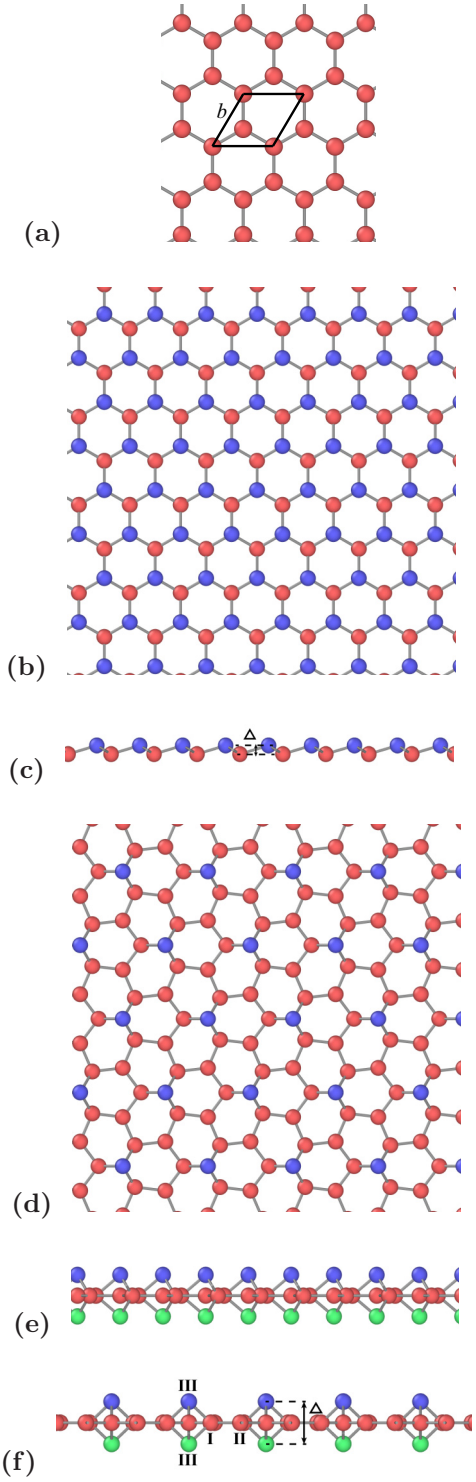

FIG. 11. Silicene structures: (a) graphitic (planar) structure, [(b) and (c)] top and edge views of the buckled structure, and [(d)–(f)] top and edge views of the $\sqrt{3} \times \sqrt{3}$ dumbbell structure.

by a significant energy release. It can be expected, therefore, that bilayer silicene should be more stable than two single layers.

Several structural forms of the bilayer silicene have been found in experiments and studied by DFT calculations, depending on the type of stacking of the two layers and whether they are planar or buckled [69,76,88–92]. Three of

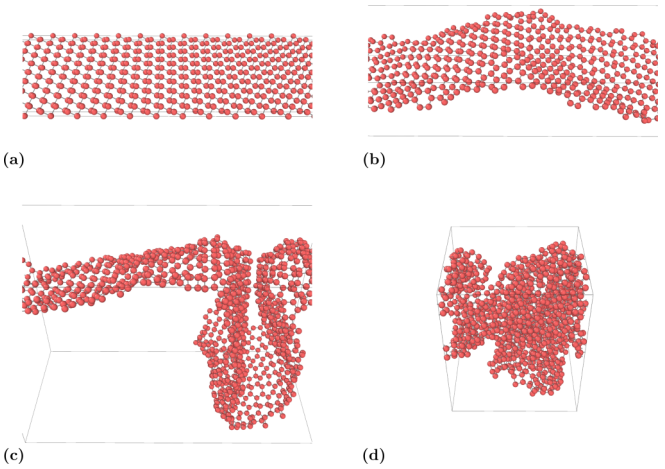

FIG. 12. Snapshots of MD simulations of a nanoribbon of buckled silicene modeled with the present interatomic potential. The temperature increases with a constant rate from 0 to 300 K over a 1-ns time period. The images show one repeat unit of the ribbon containing 1080 atoms. The time increases from (a) (initial state) to (d) (final state).

the structures, referred to as AA_p, AA′, and AB, are shown in Fig. 15. The AA_p structure is obtained by stacking two planar silicene layers (A) on top of each other and connecting them by vertical covalent bonds [Fig. 15(a)]. This structure is characterized by the geometric parameters b (side of the rhombic structural unit) and the interlayer spacing h. The bond length between Si atoms is $d_1 = b/\sqrt{3}$ within each layer and h between the layers. In the AA′ structure, both layers are buckled, and the buckling of one layer (A′) is inverted with respect to the buckling of the other layer (A) [Fig. 15(b)]. As a result, half of the interlayer distances are short, leading to the formation of covalent bonds, and the other half of the distances are longer and covalent bonds do not form. The geometric parameters of the structure are b (defined above), the in-layer bond length d_1, the interlayer bond length d_2, and the split width of each layer Δ. The distance between the layers is

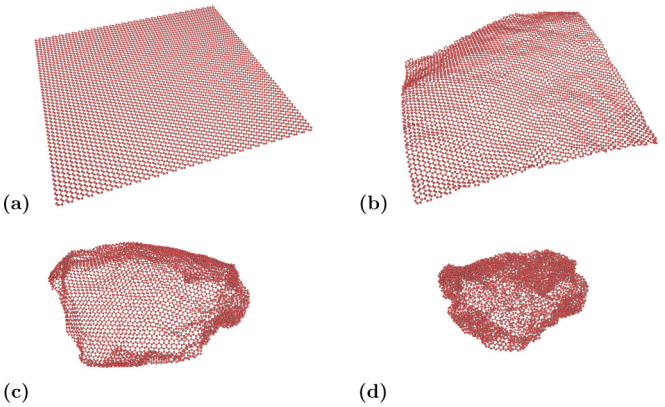

FIG. 13. Snapshots of MD simulations of a 6120-atom free-standing nanosheet (flake) of buckled silicene modeled with the present interatomic potential. The temperature increases with a constant rate from 0 to 300 K over a 0.6-ns time period [snapshots (a), (b), and (c)] followed by an isothermal anneal at 300 K [snapshot (d) taken 0.2 ns into the anneal].

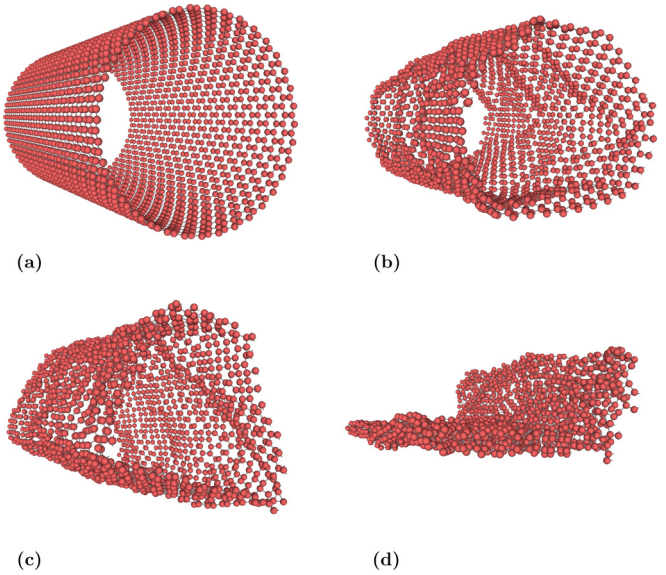

FIG. 14. Snapshots of MD simulations of a single-wall nanotube of planar silicene modeled with the present interatomic potential. The temperature increases with a constant rate from 0 to 300 K over a 2 ns time period. The images show one period of the tube (diameter 49 Å, length 122 Å, and 2160 atoms). The time increases from (a) (initial state) to (d) (final state).

$h = d_2 + \Delta$. Finally, in the AB structure, two buckled silicene layers A and B are stacked together so that half of the atoms of one layer project into the centers of the hexagonal units of the other layer [Fig. 15(c)]. The remaining half of the atoms project onto each other and form vertical covalent bonds. As with the single-layer silicenes, it has not been possible so far to isolate free-standing bilayer silicene experimentally.

The cohesive energies E_c and geometric parameters of three bilayer silicenes computed with four interatomic potentials are compared with DFT data in Table VIII. The Table also shows the energies ΔE of the buckled bilayers AA′ and AB relative to the planar bilayer AA_p. None of the potentials matches the DFT calculations accurately. However, the present potential displays the closest agreement. The MOD potential incorrectly predicts that the buckled structures AA′ and AB are more stable than AA_p (negative ΔE values), which is contrary to the DFT calculations. It should be noted that all four potentials predict virtually identical properties of the AA′ and AB silicenes. This is not very surprising: considering only nearest-neighbor bonds, the local atomic environments in the two structures are identical. Their DFT lattice parameters b are indeed the same (3.84 Å), [91] but the DFT energies are different (0.33 and 0.17 eV/atom, respectively [91]; our potential gives $\Delta E =$ 0.12 eV/atom for both). This discrepancy apparently reflects a common feature of all short-range Si potentials.

To assess thermal stability of bilayer silicenes, MD simulations were conducted for the same nanoribbon, nanoflake, and nanotube configurations as discussed above. The most stable AA_p silicene was chosen for the tests. The samples were heated up to 300 K and annealed at this temperature for 10 ns. The systems developed significant capillary waves, especially the nanoribbon, but none of them collapsed (Fig. 16). Although 10 ns is a short time in comparison with experimental times, these tests confirm that the bilayer silicene has a much greater bending rigidity and smaller reactivity in comparison with its single-layer counterpart. As such, it has a much better chance of survival in a free-standing form at room temperature.

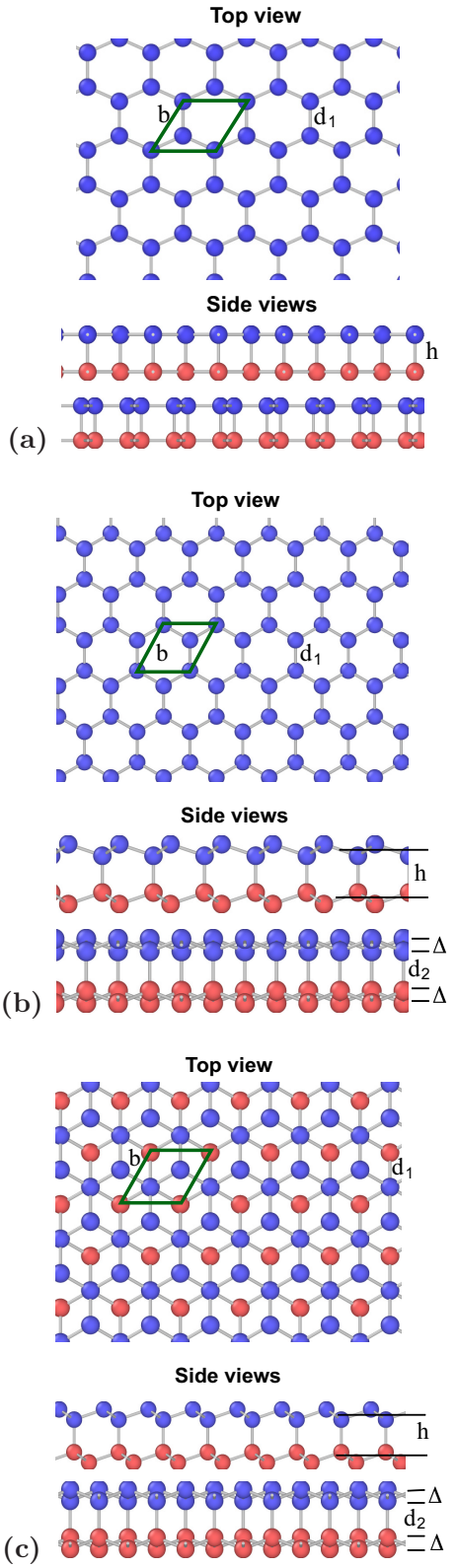

FIG. 15. Structures of bilayer silicenes: (a) AA_p, (b) AA′, and (c) AB.

TABLE VIII. Properties of three structures of bilayer silicenes computed with interatomic potentials and DFT calculations.

Property	*Ab initio*	Present	MOD[a]	MEAM[b]	SW[c]
Bilayer planar silicene AA_p:					
E_c (eV/atom)	4.16[d]; 4.27[d]	4.3067	4.2183	4.1739	3.8542
b (Å)	4.12[e]; 4.13[d] 4.14[d]	4.3264; 3.9804	4.0913	4.2685	4.1497
d_1 (Å)	2.38[d,e]; 2.39[d]	2.3641,2.3737	2.3621	2.4644	2.3958
h (Å)	2.41[d,e]	2.3916	2.4393	2.4869	2.4428
Bilayer buckled silicene AA′:					
E_c (eV/atom)		4.1866	4.2776	4.1626	3.7945
$\Delta E^{\text{buckled-planar}}$ (eV/atom)	0.33[e]	0.1201	−0.0593	0.0113	0.0597
b (Å)	3.84[e]	3.8430	3.8245	3.9155	3.8402
d_1 (Å)		2.3405	2.3311	2.4081	2.3517
d_2 (Å)		2.3543	2.3515	2.3801	2.3517
h (Å)		3.0994	3.0990	3.2101	3.1356
Δ (Å)		0.7451	0.7475	0.8300	0.7839
Bilayer buckled silicene AB:					
E_c (eV/atom)	4.10[d]; 4.25[d]	4.1866	4.2776	4.1626	3.7945
$\Delta E^{\text{buckled-planar}}$ (eV/atom)	0.17[e]	0.1201	−0.0593	0.0113	0.0597
b (Å)	3.84[d,e]; 3.86[d]	3.8429	3.8245	3.9155	3.8402
d_1 (Å)	2.32[d]	2.3405	2.3311	2.4082	2.3517
d_2 (Å)	2.51[d]; 2.54[d]	2.3543	2.3515	2.3801	2.3517
h (Å)	3.19[d]; 3.20[d]	3.0994	3.0990	3.2101	3.1359
Δ (Å)	0.66[d]; 0.68[d]	0.7451	0.7475	0.8300	0.7839

[a]Reference [7].
[b]Reference [14].
[c]Reference [1].
[d]Reference [89].
[e]Reference [91].

In additional tests, the nanoflake was heated from 300 to 1000 K in 6 ns followed by an isothermal anneal for 2 ns at 1000 K. The surface of the flake developed a set of thermally activated point defects, such as adatoms and locally buckled configurations, but the flake itself did not collapse. This again confirms the significant thermal stability of the bilayer silicene, possibly even at high temperatures. The same tests were conducted with all four potentials and the results were qualitatively similar. With the MOD potential, the initial AA_p silicene quickly transformed to the more stable buckled structure, but the system still did not collapse.

VIII. DISCUSSION AND CONCLUSIONS

Silicon is one of the most challenging elements for semiempirical interatomic potentials. It has over a dozen polymorphs that are stable at different temperatures and pressures and exhibit different coordination numbers and types of bonding ranging from strongly covalent to metallic. The diamond cubic phase displays a rather complex behavior with several possible structures of point defects, a number of surface reconstructions, and an increase in density upon melting. It is not surprising that the existing Si potentials are not nearly as successful in describing this material as some of the embedded-atom potentials for metals [93–95]. In this work, we developed a new Si potential with the goal of improving some of the properties that were not captured accurately by other potentials. For comparison, we selected three potentials from the literature that we consider most reliable [7,14] or most popular [1].

Extensive tests have shown that the present potential does achieve the desired improvements, in particular with regard to the vacancy formation energies, surface formation energies and reconstructions, thermal expansion factors, and a few other properties. The potential is more accurate, in comparison with other potentials, in reproducing the DFT data for the novel Si polymorphs h-Si_6 and Si_{24} without including them in the fitting database. However, the tests have also shown that *each* of the four potentials has its successes and failures. The present potential makes inaccurate predictions for the energies of high-lying Si polymorphs (although their atomic volumes are quite accurate), for the latent heat of melting, and for the short-range order in the liquid phase. The MOD potential [7] has its own drawbacks mentioned in Sec. I. The MEAM potential [14] grossly overestimates the phonon frequencies and thermal expansion factors, in addition to the incorrect {100} surface reconstruction. The SW potential successfully reproduces the surface energies and thermal expansion factors but predicts a positive Cauchy pressure and systematically overestimates the atomic volumes of Si polymorphs (as does the MEAM potential).

The potentials were put through a very stringent test by computing the binding energies of small Si_n clusters. Such clusters were not included in the potential fitting procedure and are traditionally considered to be out of reach of potentials unless specifically included in the fitting database. Surprisingly, the present potential, the MOD potential [7], and especially

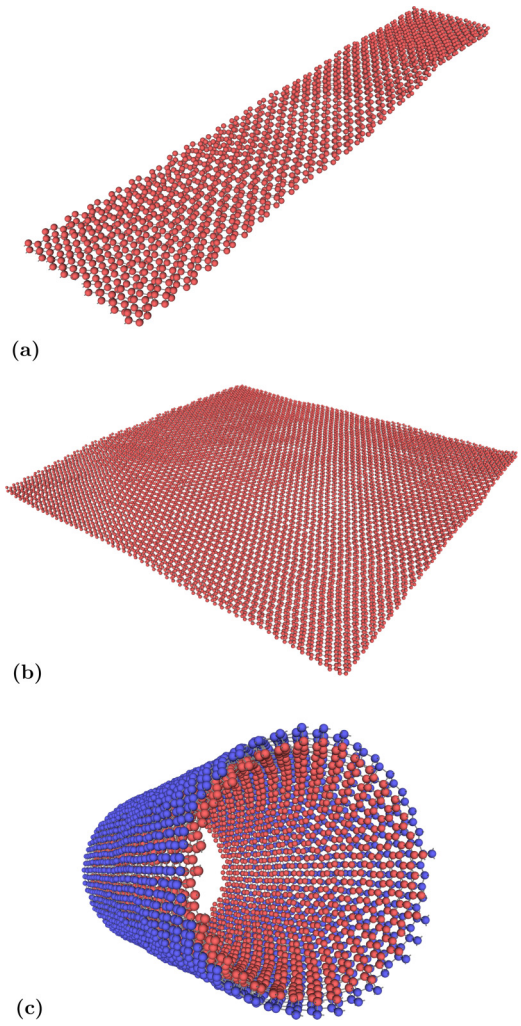

FIG. 16. Snapshots of MD simulations of the AA′ bilayer silicene after a 10 ns anneal at 300 K: (a) nanoribbon, (b) free-standing nanosheet (flake), and (c) nanotube (the two layers are shown in different colors for clarity).

the MEAM potential [14] reproduce the general trends of the cluster energies reasonably well (Fig. 10). In many cases, the ranking of the energies of different geometries for the same cluster size n agrees with first-principles calculations. The SW potential is less accurate: it systematically underbinds the clusters and makes more mistakes in the energy ordering.

Encouraged by the reasonable performance for the clusters, we applied the potentials to model single-layer and bilayer silicenes, which were not included in the potential fitting either. While none of the potentials reproduces all DFT calculations accurately, they generally perform reasonably well. One notable exception is the MOD potential, which underbinds the $\sqrt{3} \times \sqrt{3}$ dumbbell structure of the single-layer silicene and fails to reproduce the correct ground state of the bilayer silicene. Furthermore, all four potentials predict identical energies of the AA′ and AB bilayer silicenes, whereas the DFT energies are different. Other than this, the trends are captured quite well. The present potential demonstrates the best performance for the bilayer silicenes.

Experimentally, silicenes have only been found on metallic substrates. Whether they can exist in a free-standing form at room temperature remains an open question. Evaluation of their thermal stability requires MD simulations of relatively large systems for relatively long times that are not currently accessible by DFT methods. Although interatomic potentials are less reliable, they can be suitable for a preliminary assessment. The MD simulations performed in this work indicate that single-layer silicenes are unlikely to exist in a free-standing form. Their large bending compliance and chemical reactivity lead to the development of large shape fluctuations and eventually the formation of covalent bonds between neighboring surface regions at or below room temperature. By contrast, bilayer silicenes exhibit much greater bending rigidity and lower surface reactivity. Nanostructures such as nanoribbons, nanoflakes, and nanotubes remain intact at and above room temperature, at least on a 10 ns timescale. The fact that this behavior was observed with all four potentials points to the generality of these observations and suggests that free-standing bilayer silicenes might be stable at room temperature. Of course, this tentative conclusion requires validation by more detailed and more accurate studies in the future.

The four potentials discussed in this work are likely to represent the limit of what can be achieved with short-range semiempirical potentials. Further improvements can only be made by developing more sophisticated, longer-range, and thus significantly slower potentials. Analytical bond-order potentials offer one option [19,20,96]. Recent years have seen a rising interest in machine-learning potentials [97–102]. While even slower, they allow one to achieve an impressive accuracy of interpolation between DFT energies, in some cases up to a few meV/atom. However, the lack of transferability to configurations outside the training dataset is a serious issue. Whether physics-based or mathematical machine-learning type, future Si potentials will be based on much larger DFT datasets for training and testing than used in this work. This will also improve the quality by directly sampling energy-volume relations for different phases at different temperatures and pressures, deformation paths between different crystal structures, point defects, surfaces with different crystallographic orientations, as well as 2D structures and clusters.

ACKNOWLEDGMENTS

This work was supported by the U.S. Department of Energy, Office of Basic Energy Sciences, Division of Materials Sciences and Engineering, the Physical Behavior of Materials Program, through Grant No. DE-FG02-01ER45871.

[1] F. H. Stillinger and T. A. Weber, Computer simulation of local order in condensed phases of silicon, Phys. Rev. B **31**, 5262 (1985).

[2] J. Tersoff, New empirical approach for the structure and energy of covalent systems, Phys. Rev. B **37**, 6991 (1988).

[3] J. Tersoff, Empirical interatomic potential for silicon with improved elastic properties, Phys. Rev. B **38**, 9902 (1988).

[4] J. Tersoff, Modeling solid-state chemistry: Interatomic potentials for multicomponent systems, Phys. Rev. B **39**, 5566 (1989).

[5] B. W. Dodson, Development of a many-body Tersoff-type potential for silicon, Phys. Rev. B **35**, 2795 (1987).

[6] M. V. Ramana Murty and H. A. Atwater, Empirical interatomic potential for Si-H interactions, Phys. Rev. B **51**, 4889 (1995).

[7] T. Kumagai, S. Izumi, S. Hara, and S. Sakai, Development of bond-order potentials that can reproduce the elastic constants and melting point of silicon for classical molecular dynamics simulation, Comput. Mater. Sci. **39**, 457 (2007).

[8] J. Yu, S. B. Sinnott, and S. R. Phillpot, Charge optimized many-body potential for the Si/SiO_2 system, Phys. Rev. B **75**, 085311 (2007).

[9] U. Monteverde, M. A. Migliorato, and D. Powell, Empirical interatomic potential for the mechanical, vibrational and thermodynamic properties of semiconductors, J. Phys.: Conf. Ser. **367**, 012015 (2012).

[10] J. A. Martinez, D. E. Yilmaz, T. Liang, S. B. Sinnott, and S. R. Phillpot, Fitting empirical potentials: Challenges and methodologies, Curr. Opin. Solid State Mater. Sci. **17**, 263 (2013).

[11] J. F. Justo, M. Z. Bazant, E. Kaxiras, V. V. Bulatov, and S. Yip, Interatomic potential for silicon defects and disordered phases, Phys. Rev. B **58**, 2539 (1998).

[12] M. I. Baskes, J. S. Nelson, and A. F. Wright, Semiempirical modified embedded-atom potentials for silicon and germanium, Phys. Rev. B **40**, 6085 (1989).

[13] T. J. Lenosky, B. Sadigh, E. Alonso, V. V. Bulatov, T. Diaz de la Rubia, J. Kim, A. F. Voter, and J. D. Kress, Highly optimized empirical potential model of silicon, Modell. Simul. Mater. Sci. Eng. **8**, 825 (2000).

[14] S. Ryu, C. R. Weinberger, M. I. Baskes, and W. Cai, Improved modified embedded-atom method potentials for gold and silicon, Modell. Simul. Mater. Sci. Eng. **17**, 075008 (2009).

[15] M. Timonova and B. J. Thijsse, Thermodynamic properties and phase transitions of silicon using a new MEAM potential, Comput. Mater. Sci. **48**, 609 (2010).

[16] M. Timonova and B. J. Thijsse, Optimizing the MEAM potential for silicon, Modell. Simul. Mater. Sci. Eng. **19**, 015003 (2011).

[17] B. Jelinek, S. Groh, M. F. Horstemeyer, J. Houze, S. G. Kim, G. J. Wagner, A. Moitra, and M. I. Baskes, Modified embedded atom method potential for Al, Si, Mg, Cu, and Fe alloys, Phys. Rev. B **85**, 245102 (2012).

[18] B. Liu, H. Zhang, J. Tao, X. Chen, and Y. Zhang, Comparative investigation of a newly optimized modified embedded atom method potential with other potentials for silicon, Comput. Mater. Sci. **109**, 277 (2015).

[19] B. A. Gillespie, X. W. Zhou, D. A. Murdick, H. N. G. Wadley, R. Drautz, and D. G. Pettifor, Bond-order potential for silicon, Phys. Rev. B **75**, 155207 (2007).

[20] S. Y. Oloriegbe, *Hybrid bond-order potential for silicon*, Ph.D. thesis, Clemson University, Clemson, SC, 2008.

[21] A. Jain, S. Ong, G. Hautier, W. Chen, W. Richards, S. Dacek, S. Cholia, D. Gunter, D. Skinner, G. Ceder, and K. Persson, The materials project: A materials genome approach to accelerating materials innovation, APL Mater. **1**, 011002 (2013).

[22] J. E. Saal, S. Kirklin, M. Aykol, B. Meredig, and C. Wolverton, Materials design and discovery with high-throughput density functional theory: The open quantum materials database (OQMD), JOM **65**, 1501 (2013).

[23] S. Curtarolo, W. Setyawan, G. L. W. Hart, M. Jahnatek, R. V. Chepulskii, R. H. Taylor, S. Wang, J. Xue, K. Yang, O. Levy, M. J. Mehl, H. T. Stokes, D. O. Demchenko, and D. Morgan, AFLOW: An automatic framework for high-throughput materials discovery, Comput. Mater. Sci. **58**, 218 (2012).

[24] S. Curtarolo, W. Setyawan, S. Wang, J. Xue, K. Yang, R. H. Taylor, L. J. Nelson, G. L. W. Hart, S. Sanvito, M. Buongiorno-Nardelli, N. Mingo, and O. Levy, AFLOWLIB.ORG: A distributed materials properties repository from high-throughput ab initio calculations, Comput. Mater. Sci. **58**, 227 (2012).

[25] S. Plimpton, Fast parallel algorithms for short-range molecular-dynamics, J. Comput. Phys. **117**, 1 (1995).

[26] *Smithells Metals Reference Book*, edited by W. F. Gale and T. C. Totemeir, 8th ed. (Elsevier Butterworth-Heinemann, 2004).

[27] H. J. McSkimin, W. L. Bond, E. Buehler, and G. K. Teal, Measurement of the elastic constants of silicon single crystals and their thermal coefficients, Phys. Rev. **83**, 1080 (1951).

[28] L. T. Kong, Phonon dispersion measured directly from molecular dynamics simulations, Comput. Phys. Commun. **182**, 2201 (2011).

[29] G. Dolling, Lattice vibrations in crystals with the diamond structure, Inelas. Scatter. Neutr. Solids Liq. **2**, 37 (1963).

[30] G. Nilsson and G. Nelin, Study of the homology between silicon and germanium by thermal-neutron spectrometry, Phys. Rev. B **6**, 3777 (1972).

[31] A. D. Zdetsis and C. S. Wang, Lattice dynamics of Ge and Si using the Born-von Karman model, Phys. Rev. B **19**, 2999 (1979).

[32] J. Kulda, D. Strauch, P. Pavone, and Y. Ishii, Inelastic-neutron-scattering study of phonon eigenvectors and frequencies in Si, Phys. Rev. B **50**, 13347 (1994).

[33] M. J. Puska, S. Pöykkö, M. Pesola, and R. M. Nieminen, Convergence of supercell calculations for point defects in semiconductors: Vacancy in silicon, Phys. Rev. B **58**, 1318 (1998).

[34] S. Goedecker, T. Deutsch, and L. Billard, A Fourfold Coordinated Point Defect in Silicon, Phys. Rev. Lett. **88**, 235501 (2002).

[35] S. A. Centoni, B. Sadigh, G. H. Gilmer, T. J. Lenosky, T. Díaz de la Rubia, and C. B. Musgrave, First-principles calculation of intrinsic defect formation volumes in silicon, Phys. Rev. B **72**, 195206 (2005).

[36] A. F. Wright, Density-functional-theory calculations for the silicon vacancy, Phys. Rev. B **74**, 165116 (2006).

[37] J. Dabrowski and G. Kissinger, Supercell-size convergence of formation energies and gap levels of vacancy complexes in crystalline silicon in density functional theory calculations, Phys. Rev. B **92**, 144104 (2015).

[38] S. Dannefaer, P. Mascher, and D. Kerr, Monovacancy Formation Enthalpy in Silicon, Phys. Rev. Lett. **56**, 2195 (1986).

[39] Sholihun, M. Saito, T. Ohno, and T. Yamasaki, Density-functional-theory-based calculations of formation energy and concentration of the silicon monovacancy, Jpn. J. Appl. Phys. **54**, 05EA04 (2015).

[40] S. Y. Tong, H. Huang, C. M. Wei, W. E. Packard, F. K. Men, G. Glander, and M. B. Webb, Low-energy electron diffraction analysis of the Si(111)7 × 7 structure, J. Vac. Sci. Technol. A **6**, 615 (1988).

[41] R. M. Tromp, R. J. Hamers, and J. E. Demuth, Si(001) Dimer Structure Observed with Scanning Tunneling Microscopy, Phys. Rev. Lett. **55**, 1303 (1985).

[42] G.-X. Qian and D. J. Chadi, Si(111)-7 × 7 surface: Energy-minimization calculation for the dimer-adatom stacking-fault model, Phys. Rev. B **35**, 1288 (1987).

[43] A. A. Stekolnikov, J. Furthmüller, and F. Bechstedt, Absolute surface energies of group-IV semiconductors: Dependence on orientation and reconstruction, Phys. Rev. B **65**, 115318 (2002).

[44] J. Q. Broughton and X. P. Li, Phase diagram of silicon by molecular dynamics, Phys. Rev. B **35**, 9120 (1987).

[45] See Supplemental Material at http://link.aps.org/supplemental/10.1103/PhysRevB.95.224103 for a complete set of plots of the energy rate vs temperature during the melting/solidification and energy-volume relations for alternate phases of silicon.

[46] M. Müller, H. Beck, and H. J. Güntherodt, Magnetic Properties of Liquid Pd, Si, and Pd-Si Alloys, Phys. Rev. Lett. **41**, 983 (1978).

[47] Y. Waseda, K. Shinoda, K. Sugiyama, S. Takeda, K. Terashima, and J. M. Toguri, High temperature X-ray diffraction study of melt structure of silicon, Jpn. J. Appl. Phys. **34**, 4124 (1995).

[48] J. P. Gabathuler and S. Steeb, Über die Struktur von Si-, Ge-, Sn- und Pb-Schmelzen, Z. Naturforsch. A **34**, 1314 (1979).

[49] I. Štich, R. Car, and M. Parrinello, Bonding and Disorder in Liquid Silicon, Phys. Rev. Lett. **63**, 2240 (1989).

[50] W. Jank and J. Hafner, Structural and electronic properties of the liquid polyvalent elements: The group-IV elements Si, Ge, Sn, and Pb, Phys. Rev. B **41**, 1497 (1990).

[51] Y. Guo, Q. Wang, Y. Kawazoe, and P. Jena, A new silicon phase with direct band gap and novel optoelectric properties, Sci. Rep. **5**, 14342 (2015).

[52] D. Y. Kim, S. Stefanoski, O. Karakevych, and T. A. Strobel, Synthesis of an open-framework allotrope of silicon, Nat. Mater. **14**, 169 (2015).

[53] B. C. Bolding and H. C. Andersen, Interatomic potential for silicon clusters, crystals, and surfaces, Phys. Rev. B **41**, 10568 (1990).

[54] R. Fournier, S. B. Sinnott, and A. E. DePristo, Density functional study of the bonding in small silicon clusters, J. Chem. Phys. **97**, 4149 (1992).

[55] K. Raghavachari, Theoretical study of small silicon clusters: Equilibrium geometries and electronic structures of Si_n (n = 2–7,10), J. Chem. Phys. **84**, 5672 (1986).

[56] K. Raghavachari and V. Logovinsky, Structure and Bonding in Small Silicon Clusters, Phys. Rev. Lett. **55**, 2853 (1985).

[57] K. Raghavachari and C. M. Rohlfing, Bonding and stabilities of small silicon clusters: A theoretical study of Si_7–Si_{10}, J. Chem. Phys. **89**, 2219 (1988).

[58] A. Kara, H. Enriquez, A. P. Seitsonen, L. C. Lew Yan Voon, S. Vizzini, B. Aufray, and H. Oughaddou, A review on silicene—new candidate for electronics, Surf. Sci. Rep. **67**, 1 (2012).

[59] N. J. Roome and J. D. Carey, Beyond graphene: Stable elemental monolayers of silicene and germanene, Appl. Mater. Interfaces **6**, 7743 (2014).

[60] C. Grazianetti, E. Cinquanta, and A. Molle, Two-dimensional silicon: the advent of silicene, 2D **3**, 012001 (2016).

[61] T. P. Kaloni, G. Schreckenbach, M. S. Freund, and U. Schwingenschlögl, Current developments in silicene and germanene, Phys. Status Solidi RRL **10**, 133 (2016).

[62] L. C. Lew Yan Voon, J. Zhu, and U. Schwingenschlögl, Silicene: Recent theoretical advances, Appl. Phys. Rev. **3**, 040802 (2016).

[63] B. Lalmi, H. Oughaddou, H. Enriquez, A. Kara, S. Vizzini, B. Ealet, and B. Aufray, Epitaxial growth of a silicene sheet, Appl. Phys. Lett. **97**, 223109 (2010).

[64] P. Vogt, P. De Padova, C. Quaresima, J. Avila, E. Frantzeskakis, M. C. Asensio, A. Resta, B. Ealet, and G. Le Lay, Silicene: Compelling Experimental Evidence for Graphenelike Two-Dimensional Silicon, Phys. Rev. Lett. **108**, 155501 (2012).

[65] C. L. Lin, R. Arafune, K. Kawahara, N. Tsukahara, E. Minamitani, Y. Kim, N. Takagi, and M. Kawai, Structure of silicene grown on Ag(111), Appl. Phys. Exp. **5**, 045802 (2012).

[66] B. Feng, Z. Ding, S. Meng, Y. Yao, X. He, P. Cheng, L. Chen, and K. Wu, Evidence of silicene in honeycomb structures of silicon on Ag(111), Nano Lett. **12**, 3507 (2012).

[67] J. Gao and J. Zhao, Initial geometries, interaction mechanism and high stability of silicene on Ag(111) surface, Sci. Rep. **2**, 861 (2012).

[68] A. Acun, B. Poelsema, H. J. W. Zandvliet, and R. van Gastel, The instability of silicene on Ag(111), Appl. Phys. Lett. **103**, 263119 (2013).

[69] R. Arafune, C. C. Lin, K. Kawahara, N. Tsukahara, E. Minamitani, Y. Kim, N. Takagi, and M. Kawai, Structural transition of silicene on Ag(111), Surf. Sci. **608**, 297 (2013).

[70] J. Sone, T. Yamagami, Y. Aoki, K. Nakatsuji, and H. Hirayama, Epitaxial growth of silicene on ultra-thin Ag(111) films, New J. Phys. **16**, 095004 (2014).

[71] M. Neek-Amal, A. Sadeghi, G. R. Berdiyorov, and F. M. Peeters, Realization of free-standing silicene using bilayer graphene, Appl. Phys. Lett. **103**, 261904 (2013).

[72] G. R. Berdiyorov, M. Neek-Amal, F. M. Peeters, and A. C. T. van Duin, Stabilized nanosilicene within bilayer graphene, Phys. Rev. B **89**, 024107 (2014).

[73] Z. Ni, Q. Liu, K. Tang, J. Zheng, J. Zhou, R. Qin, Z. Gao, D. Yu, and J. Lu, Tunable bandgap in silicene and germanene, Nano Lett. **12**, 113 (2012).

[74] L. Tao, E. Cinquanta, D. Chiappe, C. Grazianetti, M. Fanciulli, M. Dubey, A. Molle, and D. Akinwande, Silicene field-effect transistors operating at room temperature, Nat. Nanotechnol. **10**, 227 (2015).

[75] M. Ezawa, Valley-Polarized Metals and Quantum Anomalous Hall Effect in Silicene, Phys. Rev. Lett. **109**, 055502 (2012).

[76] F. Liu, C. C. Liu, K. Wu, F. Yang, and Y. Yao, $d + id'$ Chiral Superconductivity in Bilayer Silicene, Phys. Rev. Lett. **111**, 066804 (2013).

[77] C. C. Liu, W. Feng, and Y. Yao, Quantum Spin Hall Effect in Silicene and Two-Dimensional Germanium, Phys. Rev. Lett. **107**, 076802 (2011).

[78] C. Xu, G. Luo, Q. Liu, J. Zheng, Z. Zhang, S. Nagase, Z. Gao, and J. Lu, Giant magnetoresistance in silicene nanoribbons, Nanoscale **4**, 3111 (2012).

[79] B. Peng, H. Zhang, H. Shao, Y. Xu, R. Zhang, H. Lu, D. W. Zhang, and H. Zhu, First-principles prediction of ultralow lattice thermal conductivity of dumbbell silicene: A

comparison with low-buckled silicene, Appl. Mater. Interfaces **8**, 20977 (2016).
[80] S. Cahangirov, M. Topsakal, E. Aktürk, H. Şahin, and S. Ciraci, Two- and One-Dimensional Honeycomb Structures of Silicon and Germanium, Phys. Rev. Lett. **102**, 236804 (2009).
[81] S. Cahangirov, V. O. Özçelik, A. Rubio, and S. Ciraci, Silicite: The layered allotrope of silicon, Phys. Rev. B **90**, 085426 (2014).
[82] F. Matusalem, M. Marques, L. K. Teles, and F. Bechstedt, Stability and electronic structure of two-dimensional allotropes of group-IV materials, Phys. Rev. B **92**, 045436 (2015).
[83] H. Sahin and F. M. Peeters, Adsorption of alkali, alkaline-earth, and 3d transition metal atoms on silicene, Phys. Rev. B **87**, 085423 (2013).
[84] D. Kaltsas and L. Tsetseris, Stability and electronic properties of ultrathin films of silicon and germanium, Phys. Chem. Chem. Phys. **15**, 9710 (2013).
[85] X. J. Ge, K. L. Yao, and J.-T. Lü, Comparative study of phonon spectrum and thermal expansion of graphene, silicene, germanene, and blue phosphorene, Phys. Rev. B **94**, 165433 (2016).
[86] H. Sahin, J. Sivek, S. Li, B. Partoens, and F. M. Peeters, Stone-wales defects in silicene: Formation, stability, and reactivity of defect sites, Phys. Rev. B **88**, 045434 (2013).
[87] G. R. Berdiyorov and F. M. Peeters, Influence of vacancy defects on the thermal stability of silicene: A reactive molecular dynamics study, RSC Adv. **4**, 1133 (2014).
[88] A. Resta, T. Leoni, C. Barth, A. Ranguis, C. Becker, T. Bruhn, P. Vogt, and G. L. Lay, Atomic structures of silicene layers grown on Ag(111): Scanning tunneling microscopy and noncontact atomic force microscopy observations, Sci. Rep. **3**, 2399 (2013).
[89] H. Fu, J. Zhang, Z. Ding, H. Li, and S. Meng, Stacking-dependent electronic structure of bilayer silicene, Appl. Phys. Lett. **104**, 131904 (2014).
[90] P. Pflugradt, L. Matthes, and F. Bechstedt, Unexpected symmetry and AA stacking of bilayer silicene on Ag(111), Phys. Rev. B **89**, 205428 (2014).
[91] J. Padilha and R. B. Pontes, Free-standing bilayer silicene: The effect of stacking order on the structural, electronic, and transport properties, J. Phys. Chem. C **119**, 3818 (2015).
[92] R. Yaokawa, T. Ohsuna, T. Morishita, Y. Hayasaka, M. J. S. Spencer, and H. Nakano, Monolayer-to-bilayer transformation of silicenes and their structural analysis, Nat. Commun. **7**, 10657 (2016).
[93] M. S. Daw and M. I. Baskes, Semiempirical, Quantum Mechanical Calculation of Hydrogen Embrittlement in Metals, Phys. Rev. Lett. **50**, 1285 (1983).
[94] M. S. Daw and M. I. Baskes, Embedded-atom method: Derivation and application to impurities, surfaces, and other defects in metals, Phys. Rev. B **29**, 6443 (1984).
[95] Y. Mishin, Interatomic potentials for metals, in *Handbook of Materials Modeling*, edited by S. Yip (Springer, Dordrecht, The Netherlands, 2005), pp. 459.
[96] R. Drautz, X. W. Zhou, D. A. Murdick, B. Gillespie, H. N. G. Wadley, and D. G. Pettifor, Analytic bond-order potentials for modeling the growth of semiconductor thin films, Prog. Mater. Sci. **52**, 196 (2007).
[97] T. Mueller, A. G. Kusne, and R. Ramprasad, Machine learning in materials science: Recent progress and emerging applications, in *Reviews in Computational Chemistry*, edited by A. L. Parrill and K. B. Lipkowitz (Wiley, Hoboken, NJ, 2016), Vol. 29, pp. 186.
[98] J. Behler, Perspective: Machine learning potentials for atomistic simulations, J. Chem. Phys. **145**, 170901 (2016).
[99] A. P. Bartók, M. C. Payne, R. Kondor, and G. Csányi, Gaussian Approximation Potentials: The Accuracy of Quantum Mechanics, Without the Electrons, Phys. Rev. Lett. **104**, 136403 (2010).
[100] J. Behler, and M. Parrinello, Generalized Neural-Network Representation of High-Dimensional Potential-Energy Surfaces, Phys. Rev. Lett. **98**, 146401 (2007).
[101] J. Behler, R. Martonak, D. Donadio, and M. Parrinello, Metadynamics Simulations of the High-Pressure Phases of Silicon Employing a High-Dimensional Neural Network Potential, Phys. Rev. Lett. **100**, 185501 (2008).
[102] V. Botu and R. Ramprasad, Adaptive machine learning framework to accelerate ab initio molecular dynamics, Int. J. Quant. Chem. **115**, 1074 (2015).
[103] C. Kittel, *Introduction to Sold State Physics* (Wiley-Interscience, New York, 1986).
[104] M. Timonova, B. Lee, and B. J. Thijsse, Sputter erosion of Si(001) using a new silicon MEAM potential and different thermostats, Nucl. Instrum. Methods Phys. Res., Sect. B **255**, 195 (2007).
[105] G. Lu, M. Huang, M. Cuma, and F. Liu, Relative stability of Si surfaces: A first-principles study, Surf. Sci. **588**, 61 (2005).
[106] D. J. Eaglesham, A. E. White, L. C. Feldman, N. Moriya, and D. C. Jacobson, Equilibrium Shape of Si, Phys. Rev. Lett. **70**, 1643 (1993).
[107] J. J. Gilman, Direct measurements of the surface energies of crystals, J. Appl. Phys. **31**, 2208 (1960).
[108] M. T. Yin and M. L. Cohen, Theory of static structural properties, crystal stability, and phase transformations: Application to Si and Ge, Phys. Rev. B **26**, 5668 (1982).
[109] M. G. Ganchenkova, I. A. Supryadkina, K. K. Abgaryan, D. I. Bazharov, I. V. Mutigullin, and V. A. Borodin, Influence of the ab-initio calculation parameters on prediction of energy of point defects in silicon, Mod. Electron. Mater. **1**, 103 (2015).
[110] S. Sorella, M. Casula, L. Spanu, and A. Dal Corso, *Ab initio* calculations for the β-tin diamond transition in silicon: Comparing theories with experiments, Phys. Rev. B **83**, 075119 (2011).
[111] H. Balamane, T. Halicioglu, and W. A. Tiller, Comparative study of silicon empirical interatomic potentials, Phys. Rev. B **46**, 2250 (1992).
[112] R. J. Needs and A. Mujica, First-principles pseudopotential study of the structural phases of silicon, Phys. Rev. B **51**, 9652 (1995).
[113] J. Crain, S. J. Clark, G. J. Ackland, M. C. Payne, V. Milman, P. D. Hatton, and B. J. Reid, Theoretical study of high-density phases of covalent semiconductors. I. *Ab initio* treatment, Phys. Rev. B **49**, 5329 (1994).
[114] M. Mihalkovic and M. Widom, Alloy database, http://alloy.phys.cmu.edu/, 2011.
[115] M. Methfessel and A. T. Paxton, High-precision sampling for brillouin-zone integration in metals, Phys. Rev. B **40**, 3616 (1989).

[116] M. Kaltak, J. Klimeš, and G. Kresse, Cubic scaling algorithm for the random phase approximation: Self-interstitials and vacancies in Si, Phys. Rev. B **90**, 054115 (2014).

[117] M. T. Yin, Si-III (BC-8) crystal phase of Si and C: Structural properties, phase stabilities, and phase transitions, Phys. Rev. B **30**, 1773 (1984).

[118] K. Gaál-Nagy, P. Pavone and D. Strauch, Ab initio study of the $\beta \rightarrow$ tin $\rightarrow$ Imma $\rightarrow$ sh phase transitions in silicon and germanium, Phys. Rev. B **69**, 134112 (2004).

[119] R. Biswas, R. M. Martin, R. J. Needs, and O. H. Nielsen, Complex tetrahedral structures of silicon and carbon under pressure, Phys. Rev. B **30**, 3210 (1984).

[120] E. Kaxiras and M. S. Duesbery, Free Energies of Generalized Stacking Faults in Si and Implications for the Brittle-Ductile Transition, Phys. Rev. Lett. **70**, 3752 (1993).

[121] Y. M. Juan and E. Kaxiras, Generalized stacking fault energy surfaces and dislocation properties of silicon: A first-principles theoretical study, Philos. Mag. A **74**, 1367 (1996).

[122] *Thermal Expansion: Metallic Elements and Alloys*, edited by Y. S. Touloukian, R. K. Kirby, R. E. Taylor, P. D. Desai (Plenum, New York, 1975), Vol. 12.

[123] Y. Okada and Y. Tokumaru, Precise determination of lattice parameter and thermal expanstion coefficient of silicon between 300 and 1500 K, J. Appl. Phys. **56**, 314 (1984).